Small-molecule P2RX7 activator sensitizes tumor to immunotherapy and vaccinates mouse against tumor re-challenge

Laetitia Douguet [1*], Serena Janho dit Hreich [1,4,5*], Jonathan Benzaquen [1,4,5], Laetitia Seguin [1,4], Thierry Juhel [1], Xavier Dezitter [7,9], Christophe Duranton [6], Bernhard Ryffel[12], Jean Kanellopoulos[13], Cecile Delarasse[14], Nicolas Renault [7,9], Christophe Furman [7,9], Germain Homerin [7,8], Chloé Féral [1,4], Julien Cherfils-Vicini [1], Régis Millet [7,9], Sahil Adriouch [10], Alina Ghinet [7,8,11], Paul Hofman [1,2,3,4] and Valérie Vouret-Craviari [1,4,5]

1. Université Côte d'Azur, CNRS, INSERM, IRCAN, 06108 Nice, France
2. Laboratory of Clinical and Experimental Pathology and Biobank, Pasteur Hospital, Nice, France
3. Hospital-Related Biobank (BB-0033-00025), Pasteur Hospital, Nice, France
4. FHU OncoAge, Nice, France
5. Centre Antoine Lacassagne, 06107 Nice, France
6. Université Côte d'Azur, CNRS, INSERM, LP2M, 06108 Nice, France
7. Univ. Lille, Inserm, CHU Lille, U1286 – Infinite – Institute for Translational Research in Inflammation, F-59000 Lille, France
8. Hautes Etudes d'Ingénieur (HEI), Yncréa Hauts-de-France, UC Lille, Laboratoire de chimie durable et santé, 13 rue de Toul, F-59046 Lille, France
9. Institut de Chimie Pharmaceutique Albert Lespagnol, IFR114, 3 rue du Pr Laguesse, F-59006 Lille, France
10. Normandie University, Institute for Research and Innovation in Biomedicine, F-76183 Rouen, France
11. 'Al. I. Cuza' University of Iasi, Faculty of Chemistry, Bd. Carol I, nr. 11, 700506 Iasi, Romania
12. INEM - UMR7355, Institute of Molecular Immunology and Neurogenetic, University and CNRS, Orleans, France
13. Institute for Integrative Biology of the Cell (I2BC), CEA, CNRS, Université Paris-Saclay, 91198, Gif-sur-Yvette cedex, France
14. Sorbonne Université, INSERM, CNRS, Institut de la Vision, 17 rue Moreau, F-75012 Paris, France

*Equal contribution

***Corresponding authors**:*

Dr. Valérie Vouret-Craviari or Laetitia Douguet

Running title: P2RX7 activation to fight lung cancer

ABSTRACT

Only a subpopulation of non-small cell lung cancer (NSCLC) patients responds to immunotherapies, highlighting the urgent need to develop new therapeutic strategies to improve patient outcome. We developed a new chemical positive modulator (HEI3090) of the purinergic P2RX7 receptor that potentiates αPD-1 treatment to effectively control the growth of lung tumors in transplantable and oncogene-induced mouse models and triggers long lasting antitumor immune responses. Mechanistically, the molecule stimulates dendritic P2RX7 expressing cells to generate IL-18 which leads to the production of IFN-γ by Natural Killer and $CD4^+$ T cells within tumors. Combined with immune checkpoint inhibitor, the molecule induces a complete tumor regression in 80% of LLC tumor bearing mice. Cured mice are also protected against tumor re-challenge due to a CD8-dependent protective response. Hence, combination treatment of small-molecule P2RX7 activator followed by immune checkpoint inhibitor represents a promising novel strategy that may be active against NSCLC.

KEYWORDS: Purinergic receptors, ATP, immune checkpoint inhibitor, immunosurveillance

Introduction

Despite new biological insights and recent therapeutic advances, many tumors remain resistant to treatments, leading to premature death of the patient. This is particularly true for lung cancer which is the leading cause of cancer death for men and women worldwide. The 5-year survival rate for patients with any type of lung cancer is around 20%, which dramatically drops to 6% for metastatic lung cancers. Recent advances in new effective therapies such as targeted therapies and immunotherapies have revolutionized lung cancer treatments [1]. However, it is limited to a small percentage of patients and new approaches are urgently needed to improve patient outcome.

The P2RX7 receptor (also called P2X7R) is an ATP-gated ion channel composed of three protein subunits (encoded by the *P2RX7* gene), which is expressed predominantly in immune cells and in some tumor cells [2]. Activation of P2RX7 by high doses of extracellular ATP (eATP) leads to Na^+ and Ca^{2+} influx, and, after prolonged activation, to the opening of a larger conductance membrane pore. One consequence of this large pore opening, a unique characteristic of P2RX7, is to induce cell death in eATP rich microenvironments. Noteworthy, such high doses of eATP are present in the inflammatory and tumor microenvironments [3]. P2RX7 functions are largely described in immune cells, where it is involved in NLRP3 activation to induce the maturation and secretion of IL-1β and IL-18 pro-inflammatory cytokines by macrophages and dendritic cells (DC) [4]. In line, several P2RX7 inhibitors have been developed with the aim to treat inflammatory diseases. In addition to its ability to finely tune the amplitude of the inflammatory response [5], P2RX7 has been shown to orchestrate immunogenic cell death and to potentiate DC activation and ability to present tumor antigens to T cells [6]. Among immune cells, regulatory T cells (Treg) are highly sensitive to P2RX7-induced cell death and, in the presence of eATP, P2RX7 negatively regulates their number and their suppressive function [7]. Such response can participate in P2RX7-dependent immune surveillance by unleashing the effector functions of adaptive immune T cells [8]. Therefore, P2RX7 has been proposed to represent a new positive modulator of antitumor immune response. This is in agreement with data from our group showing that P2RX7-deficient mice are more sensitive to colitis-associated cancer [9]. Also, in this model, we noticed that transplanted Lewis Lung Carcinoma tumors grew faster in line with the findings of Adinolfi and collaborators using transplanted B16 melanoma and CT26 colon carcinoma tumors [10]. Collectively, these results support the notion that P2RX7 expression by host immune cells coordinates antitumor immune response.

Capture of tumor antigens by antigen-presenting DC is a key step in immune surveillance. Activated DCs present tumor antigens to naïve T cells leading to their activation and differentiation in

effector T cells. Tumor infiltrated effector T cells and NK cells can recognize and kill tumor cells resulting in the release of additional tumor antigens and amplification of the immune response. However, this response is often inhibited by immunosuppressive mechanisms present within the tumor microenvironment (TME). Different mechanisms sustain tumor escape as the reduced immune recognition of tumors due to the absence of tumor antigens, or the loss of MHC-I and related molecules, the increased resistance of tumor cells edited by the immune responses, and the development of a favorable TME associated with the presence of immunosuppressive cytokines and growth factors (such as VEGF, TGF-β) or the expression of checkpoint inhibitors such as PD-1/PD-L1 [11]. Inhibitory checkpoint inhibitors (αPD-1/PD-L1 and anti-CTLA-4) are used in daily practice for the treatment of advanced malignancies, including melanoma and non-small-cell lung cancer (NSCLC) [12]. These antibodies reduce immunosuppression and reactivate cytotoxic effector cell functions to elicit robust antitumor responses [13,14]. High response rate to αPD-1/PD-L1 therapy is often associated with immune inflamed cancer phenotype characterized by the presence in the TME of both $CD4^+$ and $CD8^+$ T cells, PD-L1 expression on infiltrating immune and tumor cells and many proinflammatory and effector cytokines, such as IFN-γ [15]. Noteworthy, only few cancer patients achieve a response with anti-immune checkpoint administered as single-agent [16], suggesting that strategies based on combined therapies would likely enhance antitumor efficacy and immunity.

Despite the role of P2RX7 in stimulating antitumor immunity and the observation that tumor development is more aggressive in *p2rx7* deficient animals [9], it is currently not known whether P2RX7 activation can modulate tumor progression *in vivo*. The purpose of this study is to investigate the effect of a positive modulator (PM) of P2RX7 on lung tumor fate. To do so, we use syngeneic immunocompetent tumor mice models and show that activation of P2RX7 improved mice survival. Mechanistically, activation of P2RX7 leads to increased production of IL-18 in a NLRP3-dependent manner, which in turn activates NK and $CD4^+$ T cells to produce IFN-γ and consequently increases tumor immunogenicity. Finally, activation of P2RX7 combined with αPD-1 immune checkpoint inhibitor allows tumor regression, followed by the establishment of a robust immunological memory response.

Results

HEI3090 is a positive modulator of P2RX7

In order to identify positive modulator of P2RX7, 120 compounds from the HEI's proprietary chemical library were screened for their ability to increase P2RX7-mediated intracellular calcium concentration during external ATP exposure. We first produced an HEK cell line expressing the cDNA encoding for *P2RX7* from C57BL/6 origin (HEK mP2RX7) and determined the minimal dose of ATP that should be used to initiate an increase in Ca^{2+} concentration. This dose corresponds to 333 µM (not shown). We tested 5 promising compounds and identified HEI3090 as a hit (patent WO2019185868A1). HEI3090 corresponds to a pyrrolidin-2-one derivative decorated with a 6-chloropyridin-3-yl-amide in position 1 and with a 2,4-dichlorobenzylamide moiety in position 5 (Fig. 1A). HEI3090 alone showed no toxic activity (data not shown), was unable to induce intracellular Ca^{2+} variation and required the presence of eATP to rapidly and dose dependently enhance the P2RX7 mediated intracellular calcium concentration (Fig. 1B and 1C). The maximum effect of HEI3090 was observed at 250 nM, which is in the range of doses identified in pharmacokinetic analysis (Fig. 1G). HEI3090 action required the expression of P2RX7, since HEK cells transfected with empty plasmid (pcDNA6) showed no increase in intracellular calcium concentration (Fig. 1C). P2RX7 has the unique capacity to form a large pore under eATP stimulation. Large pore opening of P2RX7 was assayed with the quantification of the uptake of the fluorescent TO-PRO-3 dye. As expected, HEI3090 alone had no effect and required eATP stimulation to enhance TO-PRO-3 entry within the cells. HEI3090 increased by 2.5-fold the large pore opening (Fig. 1D). The rapid uptake of TO-PRO-3 was consistent with direct P2RX7 activation rather than ATP/P2RX7-induced cell death (Fig. 1E). We also tested HEI3090's effect on splenocytes expressing physiologic levels of P2RX7 (Fig 1F). In these immune cells, HEI3090 alone did not affect Fluo-4-AM nor TO-PRO-3 uptake. However, in the presence of eATP, HEI3090 enhanced Ca^{2+} influx and TO-PRO-3 uptake. We also showed that HEI3090 required the expression of P2RX7, since its effect was lost in splenocytes isolated from *p2rx7*$^{-/-}$ mice.

Collectively these results demonstrate that HEI3090 requires P2RX7 expression to be active and enhances eATP-induced P2RX7 activation.

HEI3090 inhibits tumor growth and enhances antitumor efficacy of αPD-1 treatment

We previously suggested that P2RX7 expression might favor the activation of immune responses [9]. We therefore evaluated the immuno-stimulatory effect and antitumor efficacy of HEI3090 *in vivo*, hypothesizing that the high level of eATP contained within the TME [17] would be sufficient to stimulate P2RX7. To do so, we used syngeneic Lewis Lung Carcinoma (LLC) and B16-F10 melanoma

cell lines expressing P2RX7 (Supplementary Figure 1). Vehicle or HEI3090 (1.5mg/kg) were administered concomitantly to LLC tumor cell injection and mice were treated daily for 11 days. Mice treated with HEI3090 displayed significantly reduced tumor growth and more than 4-fold decrease in tumor weight (Fig. 2A and Supplementary Fig. 2). We next tested the efficacy of HEI3090 to inhibit tumor growth in a therapeutic model, in which treatment started when tumor reached 10 to 15 mm^2 in volume. HEI3090 (3mg/kg), inhibited tumor growth and increased by 2-fold the median survival (Fig 2B). We also tested the effect of HEI3090 in the melanoma B16-F10 tumor mouse model and observed the same efficacy (Supplementary Fig. 3A-B).

Given the efficacy of HEI3090 to inhibit tumor growth, we next evaluated the combination of HEI3090 and αPD-1 antibody. After tumor inoculations, mice were treated daily with HEI3090 or vehicle and αPD-1 was administered at days 4, 7, 10, 13 and 16. While only 1 mouse out of the 16 mice treated with the αPD-1 alone showed a tumor regression, 13 out of the 16 mice treated with HEI3090+αPD-1 were tumor-free, suggesting that this molecule increased the efficacy of immune checkpoint inhibitor to induce effective antitumor immune responses and tumor regression (Fig. 2C). Importantly, only the combo treatment allows a long-lasting improved survival of at least 340 days (Fig. 2C, right panel). The combo treatment also increased the survival of mice grafted with B16-F10 tumors (Supplementary Fig. 3C) As illustrated in Fig 2D, we tested the combo treatment on the Kras-driven lung cancer (LSL $Kras^{G12D}$) model, which leads to adenocarcinomas 4 months after instillation of adenoviruses expressing the Cre recombinase [18]. Whereas αPD-1 treatment tends to reduce the number of ADC (Fig. 2D), HEI3090 was able to enhance αPD-1's effects in this mouse model. Indeed, tumor burden in mice treated with the combo treatment is reduced by 60% compared to mice treated with αPD-1 alone. Accordingly, the cell number per mm^2 and the number of cells positively stained for the proliferation marker Ki67 were decreased by 50% in lesion areas (Supplementary Fig. 3D). One mouse out of the 6 treated with HEI3090 and αPD-1 was protected against adenocarcinoma formation.

Dendritic cells mediate the antitumor effect of HEI3090

LLC tumor cells express an active P2RX7 since the presence of high doses of eATP leads to an increase in intracellular Ca^{2+} concentration, which is blocked by the GSK1370319A P2RX7 inhibitor [19] (Supplementary Fig. 1). To functionally investigate which cells are targeted by HEI3090, we inoculated LLC in *p2rx7*$^{-/-}$ mice and treated them with HEI3090. Whereas HEI3090 efficiently blocked LLC tumor growth in WT mice (Fig. 2A), the same treatment was inefficient in *p2rx7*$^{-/-}$ mice, as tumor growth was indistinguishable in treated or untreated groups (Fig. 3A). This result suggests that

HEI3090 requires P2RX7 expression by mouse host cells to inhibit tumor growth. The importance of immune cells was further confirmed by the demonstration that the antitumor efficacy of HEI3090 was restored after adoptive transfer of WT splenocytes into *p2rx7*$^{-/-}$ mice. Dendritic cells (DC) express P2RX7 and orchestrate antitumor immunity. Purified DC from WT spleens transferred into *p2rx7*$^{-/-}$ mice were able to restore the antitumor effect of HEI3090 (Fig. 3B). This experiment was further supported by the fact that phagocytic cells (macrophages and DC) were required for HEI3090's antitumor effect (Extended data and Supplementary Fig.4B) and that macrophages are less implicated in HEI3090's effect *in vivo* since HEI3090 is still able to inhibit tumor growth in *p2rx7*$^{fl/fl}$ LysM mice (Supplementary Fig.4C).

Flow cytometry analyses revealed that the TME of mice treated with HEI3090 were more infiltrated by immune cells than control mice (Fig. 3D). An increased infiltration of $CD8^+$ T cells was also observed in the LSL *Kras*^{G12D} lung tumor mouse model (Fig. 3E). Furthermore, we showed that HEI3090-treated mice showed higher levels of P2RX7 on DC (Supplementary Fig. 4A). Deeper characterization of immune cell infiltrate in the LLC tumor model revealed that anti-CD3 staining of tumors from HEI3090-treated mice contained 4 times more $CD3^+$ T cells than tumors from vehicle-treated mice (Fig. 3F). Whereas the proportion of $CD4^+FOXP3^+$ regulatory T cells was comparable between treated or untreated mice (Fig. 3G), we found fewer myeloid derived suppressor cells (PMN-MDSCs) after HEI3090 therapy (Fig. 3H) and higher NK/PMN-MDSC and CD4/PMN-MDSC ratios (Fig. 3I) but the treatment failed to consistently increase the CD8/PMN-MDSC ratio. We also showed that HEI3090 targets immune cells in the low immunogenic B16-F10 melanoma syngeneic mouse model, where it was able to increase anti-tumor effector cells and decrease M-MDSCs infiltration (extended data and Supplementary Fig. 5).

P2RX7 expressed by DC has been shown to link innate and adaptive immune responses against dying tumor cells upon chemotherapy–induced immunogenic cell death (ICD) and facilitate tumor antigens presentation to T cells [6]. We evaluated the capacity of HEI3090 treatment to kill tumor cells and concomitant stimulation of DC maturation. Our results showed that HEI3090 is not an immunogenic cell death inducer (see Extended data and Supplementary Fig. 6).

The two tumor cell lines used in this study express different levels of P2RX7 (Supplementary Fig. 1), yet HEI3090 required P2RX7's expressing immune cells to inhibit tumor growth in both tumor mouse models. These results demonstrate that HEI3090 controls tumor growth by recruiting and activating P2RX7-expressing immune cells, especially DC, within the TME to initiate an effective antitumor immune response.

IL-18 is produced in response to HEI3090 treatment and is required to mediate its antitumor activity

We then investigated how the activation of P2RX7 enhanced antitumor immune responses. In addition to increasing intracellular Ca^{2+} concentration and stimulating the formation of a large membrane pore (see Fig. 1), P2RX7's activation is also known to activate the NLRP3 inflammasome that leads to the activation of caspase-1 and consequently to the maturation and release of the pro-inflammatory cytokines IL-1β and IL-18. We showed that HEI3090 enhanced caspase-1 cleavage (Supplementary Fig. 7). Whereas neutralization of IL-1β did not impact HEI3090's antitumor activity, neutralization of IL-18 suppressed the antitumor effect of HEI3090 (Fig. 4A). This result was confirmed using *il18* $^{-/-}$ mice in which HEI3090 had no impact on tumor growth (Fig. 4B). IHC staining of LLC tumors from HEI3090 treated mice showed a significant intratumor amount of IL-18 compared to mice treated with the vehicle (Fig. 4C), whereas staining of tumors from *il18*$^{-/-}$ mice revealed no staining (Supplementary Fig. 8A). Concordantly, serum levels of IL-18 were statistically more abundant in mice treated with HEI3090 than in vehicle mice (Fig. 4D), and no IL-18 was detected in the serum of mice that received IL-18 neutralizing antibody. In addition, HEI3090 was unable to modulate the levels of IL-18 in *p2rx7*$^{-/-}$ mice. Moreover, HEI3090-treated WT and *p2rx7*$^{-/-}$ mice show indeed a significant difference in the release of IL-18. Finally, primary peritoneal macrophages from WT mice cultured *ex vivo* with ATP and HEI3090 produce more IL-18 than cells cultured with ATP and vehicle (Fig. 4E). IL-18 release by HEI3090 required the NLRP3 inflammasome, since its production is inhibited by the NLRP3 inflammasome-specific inhibitor (MCC950) (Fig. 4E). Moreover, we showed that HEI3090 enhanced caspase-1 cleavage (Supplementary Fig. 7) meaning that HEI3090 was able to increase IL-18 production by enhancing the activation of the NLRP3 inflammasome. Activation of P2RX7 by HEI3090 in macrophages from *p2rx7*$^{-/-}$ mice failed to increase IL-18 secretion (Supplementary Fig. 8B) and no staining was observed in LLC tumors from HEI3090 treated *p2rx7*$^{-/-}$ mice (Supplementary Fig. 8A). In agreement with the observation that HEI3090 retained its antitumor activity in mice treated with IL-1β neutralizing antibody, HEI3090 did not modify IL-1β protein levels in serum (Fig. 4D) and did not modulate IL-1β secretion in macrophages cultured *ex vivo* (Supplementary Fig. 8D).

Increased production of IL-18 was also observed in the LSL *Kras*^{G12D} lung tumor mouse model. Indeed, cells within lesions of mice treated with HEI3090 combined with αPD-1 expressed more IL-18 than mice treated with αPD-1 alone (Fig.4F). IL-18 protein levels in serum of mice that received the combo treatment were also increased by 6-fold (Fig. 4F and Supplementary Fig. 8C). As described with the LLC tumor model, HEI3090 did not impact the levels of IL-1β in this *in situ* genetic tumor mouse model (Supplementary Fig. 8F).

Collectively, these results demonstrate the antitumor effect of HEI3090 is highly dependent on P2RX7 expression and on its capacity to induce the production of mature IL-18 in the presence of eATP.

IL-18 is required to increase antitumor functions of NK and CD4$^+$ T cells

To identify which immune cells were involved in the HEI3090-induced antitumor response, we performed antibody specific cell depletion experiments. While NK and CD4$^+$ T cells depletions prevented HEI3090 treatment from inhibiting tumor growth (Fig. 5A and B), CD8$^+$ T cells depletion had no impact on HEI3090 treatment efficacy (Fig. 5A). To further study the effect of HEI3090 treatment on these subsets, we assessed their cytokine production within the TME. Analyses of tumor infiltrating immune cells first revealed that HEI3090 treatment significantly increased their capacity to produce IFN-γ (Fig. 5C). To precisely evaluate which cells in the TME produce IFN-γ, we studied the TIL sub-population and determined the ratios of IFN-γ to IL-10 production in each subset (Fig. 5D). NK and CD4$^+$ T cells were more biased to produce IFN-γ than the IL-10 immunosuppressive cytokine. CD8$^+$ T cells were relatively less prone to modification in this cytokine ratio profile upon HEI3090 treatment. In addition, two-fold more NK cells from mice treated with HEI3090 degranulate after *ex vivo* re-stimulation with LLC compared to NK from control mice (Fig. 5E), confirming their activation state, while no effect was noticeable on CD8$^+$ T cells. These phenotypic and functional analyses of intratumor immune infiltration suggested furthermore that treatment with HEI3090 stimulates CD4$^+$ T cells and NK cells' activation in the TME. Importantly, IL-18 neutralization abrogated the increase of the IFN-γ/IL-10 ratio by CD4$^+$ T cells and NK cells (Fig. 5F), suggesting that its production is a direct consequence of IL-18 release and signaling. We showed that DC and IL-18 were necessary for HEI3090's activity (Figs. 3B, 4A and B). *In vitro* stimulation of splenocytes treated with BzATP and HEI3090 did not increase IFN-γ production by T cells and NK cells indicating that its higher production in the tumor of treated mice is rather an indirect consequence of the therapy (Supplementary Fig. 9A). Concordantly, CD45$^+$ cells, CD8$^+$ T cells and NK cells in the TME of *p2rx7*$^{-/-}$ mice supplemented with WT DC showed an increase in the IFN-γ/IL-10 ratio in the HEI3090-treated mice (Supplementary Fig. 9B). This result indicates that WT DC were able to produce IL-18 after the adoptive transfer, since anti-tumor effector cells were more prone to produce IFN-γ than the IL-10 immunosuppressive cytokine.

Finally, we uncovered that HEI3090 treatment of LLC tumor bearing mice *in vivo* increased the expression of MHC-I and PD-L1 by 2.2-fold (Fig. 5G). However, when LLC cells were treated *in vitro* with HEI3090, neither MHC-I nor PD-L1 expression were increased. By contrast, IFN-γ induced the

expression of these two proteins (Supplementary Fig. 9C). Taken together, our results suggest that the *in vivo* increase of MHC-I and PD-L1 expression is a consequence of IFN-γ upregulation driven by IL-18. Finally, using the LSL *Kras*^{G12D} tumor mouse model, we showed that tumor cells from mice that received both HEI3090 and αPD-1 expressed more PD-L1 than tumor cells from mice treated with αPD-1 only (Fig. 5H). Altogether, our results indicate that HEI3090 increases IL-18 production allowing the recruitment and activation of NK and CD4$^+$ T cells and the production of IFN-γ. In turn, IFN-γ stimulates expression of MHC-I and PD-L1 on cancer cells, leading to an increased-tumor immunogenicity and an increased sensitivity to anti-immune checkpoint inhibitors.

Combined with αPD-1 antibody, HEI3090 cures mice carrying LLC tumors and allows memory immune response

Combined with an αPD-1 antibody, HEI3090 cured 80% of LLC tumor bearing mice (Fig. 2D). To determine whether cured mice developed an antitumor immune memory response, they were re-challenged with LLC tumor cells 90 days after the first inoculation and were maintained without any therapy as illustrated in Fig. 6A. All long-term recovered mice were protected from LLC re-challenge, whereas all age-matched control mice developed tumors (Fig. 6B). The re-challenged mice were still alive 150 days after the initial challenge (Fig. 6C), sustaining the hypothesis that combo treatment effectively promoted an efficient antitumor memory immune response. Our results suggested that CD8$^+$ T cells are not directly involved in the primary antitumor effect of HEI3090 (see Fig. 5A). Nevertheless, it is well characterized that these cells play a pivotal role in the host's ability to mount an antitumoral adaptative immune response [20]. To evaluate the involvement of secondary memory CD8$^+$ T cells response in these mice, we sorted CD8$^+$ cells from age-matched naïve mice or 5 months (day 150) surviving re-challenged mice (see Fig 6A) and injected them to naïve mice prior to inoculation of LLC tumor cell in a 1/1 ratio. No treatment was given to mice. In this experimental condition, tumor growth was reduced by 2-fold in mice that received CD8$^+$ T cells isolated from cured mice (Fig. 6D), indicating that the combo therapy promoted a functional immune memory response that partly depends on CD8$^+$ T cells.

We next characterized the mice that were cured for a very long period (300 days), as illustrated in Fig. 6E. First, to discriminate between dormancy and eradication of tumor cells, we depleted CD8$^+$ T cells from 300 days-old cured mice and followed mice welfare in the absence of treatment (Fig. 6F). In this condition, no tumor relapse was observed during the 40 days of the experiment and the weight of the mice remained constant, revealing that the combo treatment efficiently eliminated tumor cells. Second, since circulating CD8$^+$ T cells are actively involved in the immune memory

response [20] and participated in the HEI3090-induced antitumor response (see Fig. 6D), we investigated their involvement in the long-term memory immune response. To do so, 340 days-old cured or age-matched naïve mice were inoculated with LLC tumor cells in the absence of $CD8^+$ T cells. Both naïve- and cured- age-matched mice developed tumors (Fig 6G and 6H). However, the tumor growth was significantly reduced in cured mice and 3 out of the 6 mice did not have tumors (Fig. 6G, right panel). Cured mice survival was also significantly increased in comparison to naïve mice (Fig. 6I). Collectively, these results suggest that circulating $CD8^+$ T cells participate in the antitumor immune response induced by HEI3090.

P2RX7 is positively correlated with high infiltration of antitumor immune cells in NSCLC patients

Using the lung adenocarcinomas (LUAD) TCGA dataset, we analyzed the effect of *P2RX7* expression levels on the recruitment of cytotoxic immune cells. We clustered tumors of 80 patients with all stage (I-IV) of lung adenocarcinoma according to *P2RX7* expression and showed that high levels of *P2RX7* expression correlated with an increased-immune response in LUAD patients, characterized by a high mRNA expression of *CD274* (*PD-L1*), *IL1B*, *IL18*, a signature of primed cytotoxic T cells (defined by *CD8A*, *CD8B*, *IFN-G*, *GZMA, GZMB*, *PRF1)* (Fig. 7A). Accordingly, Gene set enrichment analysis (GSEA) demonstrated a positive correlation between high *P2RX7* expression and the well characterized established signatures of “adaptive immune response”, “T cell mediated immunity”, “cytokine production” (Fig. 7B). Furthermore, high *P2RX7* expression is correlated with high levels of *CD274 (PD-L1),* independently of the stage of the disease (Fig. 7C). Consistently, a significant reduced overall survival is observed for *P2RX7* hi, *CD274* hi and *P2RX7* hi+*CD274* hi LUAD patients (Fig. 7D), suggesting that high expression levels of *P2RX7* is sufficient to bypass immune responses in the presence of high levels of *CD274*. Such a situation is considered to benefit from anti-checkpoint blockade and/or strategies aiming to reactivate immune responses, e.g. with an activator of P2RX7. Indeed, only few cancer patients achieve a response with anti-immune checkpoint administered as single-agent and combined therapies to enhance antitumor immunity and bring a clinical benefit for patients are actively tested. We showed in this study that the combination of HEI3090 and αPD-1 is more efficient to inhibit lung tumor growth than αPD-1 alone (see Fig.2C).

Discussion

This study demonstrates for the first time that activation of the purinergic P2RX7 receptor represents a promising strategy to control tumor growth. We developed a new positive modulator of P2RX7, called HEI3090, that stimulates antitumor immunity. HEI3090 induces production of IL-18 by P2RX7 expressing immune cells, by mainly targeting DC. IL-18 drives IFN-γ production to increase tumor immunogenicity and reinforces NK and $CD4^+$ T cells immune responses and generates protective $CD8^+$ T cells responses from recidivism. Noteworthy, therapeutic association of HEI3090 with αPD-1 antibody synergizes to cure mice in the LLC syngeneic model of lung cancer and elicits an antitumor immunity. We also observed that the combo treatment is more efficient than αPD-1 alone to inhibit tumor growth in the LSL-*KRas*^{G12D} lung tumor genetic mouse model. Lung tumor regression correlates with an increased immune cell infiltration, more secretion of IL-18 within the TME and higher expression of PD-L1 by tumor cells. Furthermore, this mode of action was confirmed using the B16-F10 melanoma tumor model (Supplementary Fig 5). Collectively these results demonstrate that the antitumor activity of HEI3090 follows the same rules in all tumor models tested and highlight the strength of HEI3090 to reactivate antitumor immunity.

The design of P2RX7's modulators was based on a ligand-based approach allowing the generation of a pharmacophore model. One hundred and twenty compounds were generated and were tested for their ability to enhance P2RX7's activities; five of them were able to do so. HEI3090 was the most promising and effective compound of the five and was therefore chosen for our study. Other natural or synthetic molecules, have been described to facilitate P2RX7 response to ATP [21–23]. P2RX4 is another member of the P2X family that is described to regulate P2RX7's activities in macrophages. Recently Kawano and collaborators have shown that a positive modulator of P2RX4, the ginsenoside CK compound[25], calibrates P2RX7-dependent cell death in macrophages[26]. Therefore, we checked whether HEI3090 modulates P2RX4's activities which is not the case (data not shown).

Until now, neither of these molecules has been tested in cancer models. Moreover, attempt to facilitate P2RX7 activation in the field of oncology has been limited by the finding that P2RX7 variants expressed by some tumor cells may sustain their proliferation and metabolic activity [2]. To explore this question, we analyzed P2RX7's functional features in *ex vivo* lung cancer samples [27] and showed that P2RX7 is functional in leukocytes whereas it is nonfunctional in tumor cells. Considering that P2RX7 is a pro-apoptotic receptor, it makes sense that tumor cells express a nonfunctional receptor. Whether this non-functional receptor corresponds to the non-conformational P2RX7 (nfP2RX7), described to be expressed by tumor cells [28], remains to be determined as well as the effect of HEI3090 on nfP2RX7.

Despite the finding that P2RX7 expression by immune cells restrains tumor growth [9,10], the use of specific P2RX7 antagonists has been promoted to treat cancers on the basis that inhibition of tumor cell proliferation would be more efficient [29,30]. Considerable effort has been made to engineer specific P2RX7 antagonists [31] and two of them (A74003 and AZ10606120) inhibited B16 tumor growth in immunocompetent mice [10]. However, to our knowledge, these compounds have not been tested to treat cancer and have failed in the first clinical trials to treat inflammatory and pain-related diseases [31]. In addition, in the preclinical mouse model, we were unable to inhibit LLC and B16-F10 tumor growth when we tested the GSK1370319A compound, a well characterized P2RX7 antagonist [19] (data not shown). In line with this finding, our present results suggest that facilitation of P2XR7 is associated with efficient antitumor immunity in two different models of transplantable tumor (expressing moderate or higher level of P2RX7) as well as in the LSL-*KRas*^{G12D} genetic lung cancer mouse model. These results illustrate the view that P2RX7 activation, rather than inhibition, represent a promising strategy in cancer immunotherapy to unleash the immune responses, notably in conjunction with anti-checkpoint blockade. Therapeutic antibody represents another promising field of investigation to treat cancer. In particular, Gilbert and collaborators described an antibody against a non-functional P2RX7 variant that is promising to treat basal cell carcinoma [32]. It would be interesting to combine HEI3090 with the therapeutic P2RX7 antibody and assay the efficacy of this new combo treatment.

Antineoplastic action of eATP was previously explored using ATP administration in cancer patients and abandoned for lack of convincing results [33,34]. Extracellular ATP is naturally degraded to adenosine by ectoenzymes and adenosine is an immunosuppressive molecule [35]. To inhibit the production of adenosine, blocking antibodies against CD39 and CD73 ectoenzymes were produced and tested in mouse cancer models but also in ongoing clinical trials (NCT03454451). This strategy seems to be promising, at least in mice tumor models. In a first study, Perrot and collaborators showed that antibodies targeting human CD39 and CD73 promoted antitumor immunity by stimulating DC and macrophages which, in turn, restored the activation of effector T cells [36]. The authors also reported that the combination of anti-CD39 monoclonal antibody with oxaliplatin increased the survival of tumor bearing mice, at least for 50 days. In a second study, an independent anti-CD39 antibody was generated and tested on different mouse tumor models. This antibody alone dampened tumor growth and when combined with αPD-1, it further slowed tumor progression and 50% of the mice showed a complete rejection [37]. Mechanistically, the anti-CD39 antibody treatment led to an increased eATP levels via the P2RX7/NLRP3/IL-18 to stimulate myeloid cells. Next, the authors demonstrated that anti-CD39 antibody sensitized αPD-1 resistant tumors by increasing $CD8^+$ T cells infiltration. Our results confirm these findings but also bring new highlights. First, we showed

409 that activation of the eATP/P2RX7/NLRP3/IL-18 pathway by HEI3090 increased long lasting immune
410 responses when combined with αPD-1 antibody. Second, we demonstrated that the endogenous
411 eATP levels present in the TME was sufficient to enhance P2RX7's activation in the presence of
412 HEI3090. These conditions are ideal to allow P2RX7 activation where it is needed and avoid the
413 possible adverse effects associated with a systemic increase of ATP levels, such as the one observed
414 in response to anti-CD39 and -CD73 antibodies.

415 It was shown that eATP attracts DC precursors towards the TME and promotes their activation
416 state and their capacity to present antigen [38,39]. During the course of this study, we showed that
417 HEI3090 targets P2RX7 expressing immune cells, especially phagocytic cells, such as macrophages
418 and DCs (Supplementary Fig 4B). Between macrophages and dendritic cells, dendritic cells were the
419 most promising candidate; they express high levels of P2RX7, they are able to release IL-18, they are
420 professional antigen-presenting cells able to induce a potent anti-tumor immune response. We
421 therefore tested their involvement by doing an adoptive transfer of WT DC in *p2rx7*$^{-/-}$ mice. Doing so,
422 we restored responsiveness to HEI3090 (Fig. 3B). We also observed that cDC CD4^{+} T from mice
423 treated with HEI3090 expressed higher levels of P2RX7 (Supplementary Fig. 4A). Collectively, these
424 results demonstrated that DCs mediate HEI3090's antitumor activity, but macrophages may have a
425 secondary role in this effect.

426 Intriguingly, we did not observe an enhanced production of mature IL-1β in mice treated with
427 HEI3090 (Fig. 4D). This was unexpected as secretion of mature IL-1β depends on the ATP/P2RX7-
428 induced NLRP3 inflammasome activation as well [40]. However, unlike IL-1β, the inactive precursor
429 form of IL-18 is constitutively expressed in most human and animal cells. Whether this explanation is
430 sufficient alone to account for this differential IL-1β/IL-18 production is currently not known.

431 Whereas IL-1β is described to induce immune escape [41], IL-18 is involved in Th1 polarization and
432 NK cell activation. We showed here that IL-18 produced in response to HEI3090 treatment
433 orchestrated the antitumor immune response by driving IFN-γ production by NK and CD4^{+} T cells. This
434 is in line with the well-known IFN-γ stimulating activity of IL-18 (originally designated as IFN-γ-
435 inducing factor), and with its Th1 and NK cells stimulating activity [42,43]. Protective effect of IL-18, but
436 also the activation of NLRP3, have been previously reported in various mouse cancer models [44,45]
437 NLRP3 activation in DCs as well as IL-18 have been linked to better prognosis, to drive anti-tumor
438 immunity and to enhance the efficacy of immunotherapies in different tumor models [46]. In fact,
439 when we combined HEI3090 with an αPD-1 antibody, we observed that the combo therapy
440 efficiently controlled tumor burden in the 3 cancer models studied. Notably, the combo treatment
441 cured 80% of LLC tumor bearing mice and very interestingly, cured mice developed an antitumor
442 memory response.

CD8 memory T cells, comprising the circulating memory pool – composed of effector memory (T_{EM}) and central memory (T_{CM}) cells - and the tissue resident (T_{RM}) pool, play crucial roles in antitumor memory responses [47]. We showed that circulating $CD8^+$ T cells participated in cancer immunosurveillance after HEI3090 treatment (Fig. 6D). However, this $CD8^+$ T cells pool cannot be responsible for the entire response, since antitumor responses were still effective when $CD8^+$ T cells were depleted (Fig. 6G). These results suggest that other immune cells participate in local cancer surveillance. Possible candidates are the non-recirculating $CD8^+$ T_{RM} cells. The persistence of T_{RM} cells in tissues has been shown to depend on signaling programs driven by TGFβ and Notch-dependent signaling signature. Whether HEI3090 directly stimulates those programs remains to be determined but we observed, using HEK mP2RX7 cells, that HEI3090 enhanced ATP-stimulated ERK pathways (data not shown). Our results are also compatible with a role for $CD4^+$ T memory cells and the setup of a humoral response, in which B lymphocytes produce antibody against tumor cells.

Therapy with different αPD-1/PD-L1 antibodies was approved in NSCLC in the first- and second-line settings. However, a significant fraction of patients does not benefit from the treatment (primary resistance), and some responders relapse after a period of response (acquired resistance) [48]. Expression of PD-L1 *per se* is not a robust biomarker with a predictive value since the αPD-L1 response has also been observed in some patients with PD-L1-negative tumors. Improvement of patient management for immunotherapy undoubtedly relies on the identification of such predictive markers. Using TCGA data set, we uncovered that *P2RX7* expression is correlated to *CD274* (PD-L1) expression and "hot" immunophenotype signatures in NSCLC patients. In addition, patients with high *P2RX7* and low *CD274* or high *CD274* and *low P2RX7* have a better overall survival than patients with high *CD274* and high *P2RX7*. This result suggests that immunotherapies may be efficient in double positive patients and questions the ability of P2RX7 to represent a valuable biomarker for αPD-1/PD-L1 therapies. In this context, we showed in another study [27] that the expression of *P2RX7B* splice variant in tumor immune cells is associated with less infiltrated tumors in lung adenocarcinoma. Mechanistically, we observed that the differential expression of the *P2RX7B* splice variant in immune cells within tumor area correlates with the expression of a less functional P2RX7 and lower leukocytes recruitment into LUAD.

To our knowledge, this is the first study demonstrating that a small-molecule activator of P2RX7 boosts immune surveillance by unleashing the effector functions of adaptive immune T cells and improving the efficacy of αPD-1 treatment. This therapeutic strategy holds new hopes for cancer patients. By increasing tumor immunogenicity, it could first increase the number of patients eligible to immunotherapies and second, it could also be used as a neoadjuvant or adjuvant therapies of locally advanced lung tumors.

Methods section

Mice

This study was approved by the Institutional Care and Use Committee of the University of Nice-Sophia Antipolis. Animal protocols were approved by the committee for Research and Ethics of the PACA region (CIEPAL azur) and followed the European directive 2010/63/UE, in agreement with the ARRIVE guidelines. *P2rx7*$^{-/-}$ (B6.129P2-*P2rx7*^{tm1Gab}/J) and *il18*$^{-/-}$ mice were from the Jackson Laboratory. LSL-*KRas*^{G12D} tumor lung model has been described in [18]. The generation of C57BL/6 mice harboring constitutive and myeloid specific targeted disruption of the *p2rx7* gene is described in the extended data section. Control C57BL/6J OlaHsD female (WT mouse) were supplied from Envigo (Gannat, France).

In vivo treatments

We used Lewis Lung Carcinoma (ATCC CRL-1642) and the melanoma B16-F10 (ATCC CRL-6475) tumor cell lines. Cells were routinely checked for mycoplasma contamination and used between passages 7 to 15. Five x 10^5 tumors cells were injected s.c. into the left flank of WT mice. Pharmacokinetic analysis (Figure 1G), to characterize the clearance of HEI3090 showed that after a period of 18 h HEI3090 concentration is < 10 nM. Therefore, we have decided to inject HEI3090 daily. Mice were treated i.p. with vehicle (PBS, 10% DMSO) or with HEI3090 (1.5 mg/kg in PBS, 10% DMSO) which corresponds to the highest soluble dose. For therapeutic settings treatment started at day 3, when tumor reached approximately 10 to 15 mm^2, for a maximum of 20 days and mice received vehicle or HEI3090 (3 mg/kg in PBS, 10% DMSO) daily. Depleting and neutralizing antibodies from BioXCell were given i.p. in the right flank at days -1, 3, 7 and 10. We used anti-IL-1β (clone B122, 200 µg per injection), anti-IL-18 (clone YIGIF74-1G7, 200 µg per injection), anti-CD8 (clone 53-6.7 200 µg/injection), anti-CD4 (clone GK1.5, 200 µg per injection) and anti-NK1.1 (clone PK136, 300 µg per injection). αPD-1 antibody (clone RPM1-4, BioXCell) was given i.p. at 200 µg per injection at days 4, 7, 10 and 13 (or as stated in the legend of the figure) post tumor cell inoculation. αPD-1 and HEI3090 were injected separately, with at least 30 min delay between the two injections. 200 µL liposome clodronate (Liposoma) were injected i.p. 3 days before LLC tumor cell inoculation in WT mice and then every 3 days, at least 1 hour before HEI3090 treatment after the treatment started. $CD8^+$ T cells were sorted from peripheral lymph nodes of cured or naïve WT mice with Dynabeads® Untouched™ Mouse CD8 Cells (Invitrogen) according to the supplier's instructions. 5.10^5 $CD8^+$ T cells were adoptively transferred into 8 weeks-old naïve WT mice (i.v.) one day before tumor inoculation. 5.10^5 LLC cells were injected s.c. into the left flank of these mice and given no further treatment.

Adoptive transfer in *p2rx7* deficient mice

Spleens from WT C57BL/6J female mice were collected and digested in RPMI 1640 medium containing 5% FCS, 1 mg/ml collagenase IV (Sigma-Aldrich), and 50 U/ml DNase I (Roche) for 7 min at 37°C. Single-cell suspensions of spleens were prepared by passage through 100 µm cell strainers (BD Biosciences) and counted. For WT DCs isolation, spleens were digested with the spleen dissociation kit (Miltenyi Biotech) and isolated with the CD11c Microbeads UltraPure (Miltenyi biotech) according to the supplier's instructions. 5.10^6 splenocytes or $1.2.10^6$ DCs were injected i.v. in *p2rx7*$^{-/-}$ mice one day before subcutaneous injection of 5.10^5 LLC cells into the left flank. Mice were treated i.p. every day for 12 days with vehicle (PBS, 10% DMSO) or with HEI3090 (1.5 mg/kg in PBS, 10% DMSO). At day 12, tumors were collected, weighted and digested, when flow cytometry analyses were done.

Flow cytometry and antibodies

Tumors were mechanically dissociated and digested with 1 mg mL^{-1} collagenase A and 0.1 mg mL^{-1} DNase I for 20 min at 37°C. Then single cell suspensions of tumors were prepared by passage through 100 µM cell strainers (BD Biosciences). Surface staining was performed by incubating cells on ice, for 20 min, with saturating concentrations of labeled Abs in PBS, 5% FCS and 0.5% EDTA. After blocking Fc receptors using anti-CD16/32 (2.4G2) antibodies, cells were stained with the appropriate combination of antibodies (see Supplementary Table 1). The transcription factor staining Buffer Set (eBioscience) was used for the FoxP3 staining. For intracellular cytokines, staining was performed after stimulation of single-cell suspensions with Phorbol 12-myristate 13-acetate (PMA at 50 ng mL^{-1}, Sigma), ionomycin (0.5 µg mL^{-1}, Sigma) and 1 µL mL^{-1} Golgi Plug™ (BD Biosciences) for 4 h at 37°C 5% CO_2. Cells were incubated with Live/Dead Blue stain (Invitrogen), according to the manufacturer's protocol prior to Ab surface staining. Then, intracellular staining was performed using Cytofix/Cytoperm™ kit (BD biosciences) following the manufacturer's instructions. The production of IFN-γ and IL-10 was simultaneously analyzed in $CD45^+$, NK, $CD4^+$ T or $CD8^+$ T cells. Data files were acquired and analyzed on Aria III using Diva software (BD Biosciences) or on the CytoFlex LX (Beckman Coulter) and analyzed using FlowJo software (LLC).

Immunohistological analysis of tumors

Collected tumors or lungs were processed as previously described [9]. We used the following antibodies: anti-CD3 and anti-CD8 (Roche, 790-4341, 750-4460 respectively), anti-IL-18 (BioVision, dil 1/200), and αPD-L1 (Dako, clone 22C3, dil 1/50), anti-Ki67 (Abcam, clone sp6, dil 1/100). After staining, slides were captured and analyzed using NDP view2 software. For the analyses, 5 zones per tumor were randomly selected and cells were counted using Figdi software. Results are expressed as number of positive cells per total cell number.

Characterization of lesions in the LSL *KRas*^{G12D} mouse model

At the end of the treatment mice were sacrificed, exsanguinated and lungs processed for histologic and immunological analyses as described here [49]. After deparaffinization, HE stains were performed and slides were captured and analyzed using NDP view2 software. Tumor burden was calculated by determining the mean of total tumor area per lung using the NDPview2 software. To count the cells and determine the percentage of Ki67 positive cells within lesions, 10 lesions per lung, from grade 2 to 5 according to the Sutherland scoring [50], were randomly selected, their perimeter was determined, and positive and negative nuclei were counted using Fidgi software. Results are expressed as number of cells per mm^2 and the percentage of Ki67 positive cells.

Ex vivo macrophages stimulation

Peritoneal lavage was done with RPMI 1640 medium on WT or *p2rx7*$^{-/-}$ mice. 4.10^5 macrophages were seeded in a 96 well plate overnight in RPMI 1640 containing 10% FBS, 2% sodium pyruvate, 1% penicillin/streptomycin and 50 µM β-mercaptoethanol. After 2 washes with the complete medium, cells were primed for 4 hours with 100 ng/ml LPS (Sigma-Aldrich) at 37 ˚C and then stimulated for 30 minutes at 37 ˚C with ATP (Sigma-Aldrich) with or without 50 µM of HEI3090 or with 10 µM nigericin. When indicated, NLRP3 inflammasome was inhibited with 1 µM of MCC950 (Invivogen) for 1 hour at 37 ˚C before cell stimulation.

Supernatants were collected and stored at -80˚C before cytokine detection by ELISA using mouse IL-1 beta/IL-1F2 (R&D) and IL-18 (MBL) according to the supplier's instructions.

Cells were lysed with Laemmli buffer (10% glycerol, 3% SDS, 10 mM Na_2HPO_4) with protease inhibitor cocktail (Roche). Proteins were separated on a 12% SDS-PAGE gel and electro transferred onto PVDF membranes which were blocked for 30 minutes at RT with 3% bovine serum albumin (BSA). Membranes were incubated with primary antibodies diluted 1/1000 at 4˚C overnight. The following antibodies were used: anti-NLRP3 (clone Cryo-2, Adipogen) anti-ASC (clone AL177, Adipogen), anti-caspase-1 (clone Casper-1, Adipogen) and anti-β-actin (Biorad). Secondary antibodies (Sigma-Aldrich) were incubated for 1 hour at RT. Immunoblot detection was achieved by exposure with a chemiluminescence imaging system (PXI Syngene, Ozyme) after membrane incubation with ECL (Immobilon Western, Millopore). The bands intensity values were normalized to that of β-actin using ImageJ software.

Calcium uptake assay

20.10^3 HEK293T-mP2RX7$^{C57BL/6J}$ or HEK293T-pcDNA6 cells were seeded per well on a poly-L-Lysine (Sigma-Aldrich) 96 well-coated plate in complete medium. 24 hours later, cells were washed in sucrose buffer (300 mM sucrose, 5 mM KCl, 1mM $MgCl_2$, 1mM $CaCl_2$, 10 mM Glucose, 20 mM HEPES, pH 7-7.4) and incubated for 1 hour at 37 °C with 1 µM of Fluo-4 AM (Life Technologies). Cells were washed once with PBS+5% FBS then twice with the sucrose buffer. Fluo-4 AM fluorescence was read

on a Xenius, microplate reader (SAFAS) at 485/528 nm at 37 °C. After 3 minutes of baseline readings, 333 µM of ATP (Sigma-Aldrich) were added with or without various concentrations of HEI3090. For the assay on splenocytes, spleens were digested with the spleen dissociation kit (Miltenyi Biotech). 5.10^5 splenocytes were seeded per well on a 96-well plate in sucrose buffer and incubated for 30 minutes at RT with 1 µM of Fluo-4-AM.

TO-PRO-3 uptake assay

30.10^3 HEK293T-mP2RX7$^{C57BL/6J}$ or HEK293T-pcDNA6 cells were seeded per well on a poly-L-Lysine (Sigma-Aldrich) black clear bottom 96 well-coated plate (Perkin Elmer) in complete medium. 24 hours later, cells were washed twice in sucrose buffer (300 mM sucrose, 5 mM KCl, 1mM $MgCl_2$, 1mM $CaCl_2$, 10 mM Glucose, 20 mM HEPES, pH 7-7.4). 1 µM of TO-PRO-3 (Life Technologies) was added in the sucrose buffer. TO-PRO-3 fluorescence was read on a Xenius, microplate reader (SAFAS) at 550/660 nm at 37°C. After 10 minutes of baseline readings, 250 µM of ATP (Sigma-Aldrich) were added with or without various concentrations of HEI3090. Alternatively, percentage of TO-PRO-3$^+$ cells was analyzed on non-adherent cells by flow cytometry.

Cell viability

Colorimetric assay based on XTT (Roche) was used to quantify the viability of tumor cells treated with 1 mM of BzATP and 50 µM of HEI3090. LLC cells were treated for 16h and B16-F10 for 3h. Cellular viability was determined as described in the supplier's protocol.

***In vivo* assay for immunogenic cell death**

B16-F10 were exposed to 3mM ATP and 50 µM HEI3090 for 3 hours at 37 °C. Cells were then washed and resuspended in PBS and cell death was determined with trypan blue. Dying B16-F10 cells reached 97% in this assay. One.10^5 dying cells were injected *s.c.* into the right flank of WT mice (in 200 µL PBS). Control mice received 200 µL PBS into the right flank. Seven days later, mice were challenged with live $5x10^5$ B16-F10 cells into the left flank. Tumor growth was routinely monitored at both injection sites.

Synthesis of HEI3090

Starting materials are commercially available and were used without further purification (suppliers: Carlo Erba Reagents S.A.S., Thermo Fisher Scientific Inc., and Sigma-Aldrich Co.). Intermediates were synthesized according to the methods described in the literature [28]. Melting points were measured on the MPA 100 OptiMelt® apparatus and are uncorrected. Nuclear magnetic resonance (NMR) spectra were acquired at 400 MHz for ^{1}H NMR and at 100 MHz for ^{13}C NMR, on a

Varian 400-MR spectrometer with tetramethylsilane (TMS) as internal standard, at 25 °C. Chemical shifts (δ) are expressed in ppm relative to TMS. Splitting patterns are designed: s, singlet; d, doublet; dd, doublet of doublet; t, triplet; m, multiplet; sym m, symmetric multiplet; br s, broaden singlet; br t, broaden triplet. Coupling constants (J) are reported in Hertz (Hz). Thin layer chromatography (TLC) was realized on Macherey Nagel silica gel plates with fluorescent indicator and were visualized under a UV-lamp at 254 nm and 365 nm. Column chromatography was performed with a CombiFlash Rf Companion (Teledyne-Isco System) using RediSep packed columns. IR spectra were recorded on a Varian 640-IR FT-IR Spectrometer. Elemental analyses (C, H, N) of new compounds were determined on a Thermo Electron apparatus by 'Pôle Chimie Moléculaire-Welience', Faculté de Sciences Mirande, Université de Bourgogne, Dijon, France. LC-MS was accomplished using an HPLC combined with a Surveyor MSQ (Thermo Electron) equipped with APCI source.

The synthesis of the title compound was accomplished starting from L-pyroglutamic acid also known as the "forgotten amino acid", bio-sourced affordable raw material (Fig. 1A). After simple esterification of the L-pyroglutamic acid, the resulting methyl pyroglutamate was reacted with 2,4-dichlorobenzylamine in presence of catalytic amount or zirconium (IV) chloride in solvent-less conditions to provide pyroglutamide (HEI2313) in 90% yield. To obtain *(S)-N^1-(6-chloropyridin-3-yl)-N^2-(2,4-dichlorobenzyl)-5-oxopyrrolidine-1,2-dicarboxamide* (HEI3090), a mixture of pyroglutamide (HEI2313) (1.86 g, 6.48 mmol) and 2-chloro-5-isocyanatopyridine (1.00 g, 6.48 mmol) in toluene was refluxed for 24 hours under nitrogen atmosphere and magnetic stirring. After cooling to rt, the mixture has been concentrated *in vacuo* and the resulting crude has been purified by column chromatography (CH_2Cl_2 / MeOH: 1/0 to 9/1) to afford pure HEI3090 as a white powder in 54% yield (1.62 g, 3.51 mmol). mp 187-190 °C (MeOH); TLC R*f* (CH_2Cl_2/MeOH: 95/5) 0.8; ^{1}H NMR ($CDCl_3$, 400 MHz) δ ppm 2.21-2.37 (m, 2H, CH_2CH$_2$CH), 2.59-2.68 (m, 1H, CH$_2$CH_2CH), 2.99-3.10 (m, 1H, CH$_2$CH_2CH), 4.49 (dd, *J* = 15.2, 6.2 Hz, 1H NHCH_2), 4.55 (dd, *J* = 15.2, 6.2 Hz, 1H, NHCH_2), 4.77 (dd, *J* = 7.2, 2.8 Hz, 1H, CH$_2$CH$_2$CH), 6.65 (br t, *J* = 6.2 Hz, 1H, N*H*CH$_2$), 7.22 (dd, *J* = 8.1, 2.0 Hz, 1H, Ar*H*), 7.29 (d, *J* = 8.6 Hz, 1H, Ar*H*), 7.33 (d, *J* = 8.1 Hz, 1H, Ar*H*), 7.38 (d, *J* = 2.0 Hz, 1H, Ar*H*), 7.92 (dd, *J* = 8.6, 2.5 Hz, 1H, Ar*H*), 8.49 (d, *J* = 2.5 Hz, 1H, Ar*H*), 10.66 (br s, 1H, N*H*Ar); ^{13}C NMR ($CDCl_3$,100 MHz) δ ppm 21.4 (CH$_2$), 32.4 (CH$_2$), 41.4 (CH$_2$), 59.2 (CH), 124.3 (CH), 127.5 (CH), 129.5 (CH), 130.2 (CH), 130.9 (CH), 133.1 (C), 133.6 (2 C), 134.2 (C), 141.3 (CH), 146.2 (C), 150.3 (C), 170.0 (C), 177.7 (C); IR (neat): ν cm^{-1} 3271, 3095, 1720, 1655, 1594, 1542, 1464, 1217, 1104, 829.

Statistical analyses

All analyses were carried out using Prism software (GraphPad). Mouse experiments were performed on at least n = 5 individuals, as indicated in Fig legends. Mice were equally divided for treatments and controls. Data were represented as mean values and error bars represent SEM.

645 Mann-Whitney, t test and Mantel Cox test were used to evaluate the statistical significance between
646 groups. The corresponding tests and P -values were mentioned in the legend of each Figure. For
647 survival analysis, patients were separated based on optimal cut-off of the expression value of the
648 marker determined using KMplot.

Data Availability

All relevant data are available from the authors

652

653 **References**

654 1. Schrank, Z. *et al.* Current molecular-targeted therapies in NSCLC and their mechanism of
655 resistance. *Cancers (Basel).* **10**, E224 (2018).

656 2. Benzaquen, J. *et al.* Alternative splicing of P2RX7 pre-messenger RNA in health and diseases:
657 Myth or reality? *Biomed. J.* **42**, 141–154 (2019).

658 3. Pellegatti, P. *et al.* Increased level of extracellular ATP at tumor sites: In vivo imaging with
659 plasma membrane luciferase. *PLoS One* **3**, 1–9 (2008).

660 4. Perregaux, D. G., McNiff, P., Laliberte, R., Conklyn, M. & Gabel, C. A. ATP Acts as an Agonist to
661 Promote Stimulus-Induced Secretion of IL-1β and IL-18 in Human Blood. *J. Immunol.* **165**,
662 4615–4623 (2000).

663 5. Cesaro, A. *et al.* Amplification loop of the inflammatory process is induced by P2X 7R
664 activation in intestinal epithelial cells in response to neutrophil transepithelial migration. *Am.*
665 *J. Physiol. - Gastrointest. Liver Physiol.* **299**, G32-42 (2010).

666 6. Ghiringhelli, F. *et al.* Activation of the NLRP3 inflammasome in dendritic cells induces IL-1B-
667 dependent adaptive immunity against tumors. *Nat. Med.* **15**, 1170–1178 (2009).

668 7. Rissiek, B., Haag, F., Boyer, O., Koch-Nolte, F. & Adriouch, S. ADP-ribosylation of P2X7: A
669 matter of life and death for regulatory T cells and natural killer T cells. *Curr. Top. Microbiol.*
670 *Immunol.* **384**, 107–126 (2014).

671 8. Hubert, S. *et al.* Extracellular NAD+ shapes the Foxp3+ regulatory T cell compartment through
672 the ART2-P2X7 pathway. *J. Exp. Med.* **207**, 2561–2568 (2010).

673 9. Hofman, P. *et al.* Genetic and pharmacological inactivation of the purinergic P2RX7 receptor
674 dampens inflammation but increases tumor incidence in a mouse model of colitis-associated
675 cancer. *Cancer Res.* **75**, 835–845 (2015).

676 10. Adinolfi, E. *et al.* Accelerated tumor progression in mice lacking the ATP receptor P2X7. *Cancer*
677 *Res.* **75**, 635–644 (2015).

678 11. Vesely, M. D., Kershaw, M. H., Schreiber, R. D. & Smyth, M. J. Natural Innate and Adaptive
679 Immunity to Cancer. *Annu. Rev. Immunol.* **29**, 235–271 (2011).

680 12. Hughes, P. E., Caenepeel, S. & Wu, L. C. Targeted Therapy and Checkpoint Immunotherapy
681 Combinations for the Treatment of Cancer. *Trends Immunol.* **37**, 462–476 (2016).

682 13. Postow, M. A. *et al.* Peripheral T cell receptor diversity is associated with clinical outcomes
683 following ipilimumab treatment in metastatic melanoma. *J. Immunother. Cancer* **3**, 23 (2015).

684 14. Topalian, S. L. *et al.* Immunotherapy: The path to win the war on cancer? *Cell* **161**, 185–186
685 (2015).

686 15. Chen, D. S. & Mellman, I. Elements of cancer immunity and the cancer-immune set point.
687 *Nature* **541**, 321–330 (2017).

688 16. Eggermont, A. M. M., Maio, M. & Robert, C. Immune checkpoint inhibitors in melanoma
689 provide the cornerstones for curative therapies. *Semin. Oncol.* **42**, 429–435 (2015).

690 17. Di Virgilio, F., Sarti, A. C., Falzoni, S., De Marchi, E. & Adinolfi, E. Extracellular ATP and P2
691 purinergic signalling in the tumour microenvironment. *Nat. Rev. Cancer* **18**, 601–618 (2018).

692 18. DuPage, M., Dooley, A. L. & Jacks, T. Conditional mouse lung cancer models using adenoviral
693 or lentiviral delivery of Cre recombinase. *Nat. Protoc.* **4**, 1064–1072 (2009).

694 19. Homerin, G. *et al.* Pyroglutamide-Based P2X7 Receptor Antagonists Targeting Inflammatory
695 Bowel Disease. *J. Med. Chem.* **63**, 2074–2094 (2020).

696 20. Mittal, D., Gubin, M. M., Schreiber, R. D. & Smyth, M. J. New insights into cancer

immunoediting and its three component phases-elimination, equilibrium and escape. *Curr. Opin. Immunol.* **27**, 16–25 (2014).

21. Fischer, W., Urban, N., Immig, K., Franke, H. & Schaefer, M. Natural compounds with P2X7 receptor-modulating properties. *Purinergic Signal.* **10**, 313–326 (2014).

22. Di Virgilio, F., Giuliani, A. L., Vultaggio-Poma, V., Falzoni, S. & Sarti, A. C. Non-nucleotide agonists triggering P2X7 receptor activation and pore formation. *Front. Pharmacol.* **9**, 39 (2018).

23. Bidula, S. M., Cromer, B. A., Walpole, S., Angulo, J. & Stokes, L. Mapping a novel positive allosteric modulator binding site in the central vestibule region of human P2X7. *Sci. Rep.* **9**, 1–11 (2019).

24. Bidula, S., Dhuna, K., Helliwell, R. & Stokes, L. Positive allosteric modulation of P2X7 promotes apoptotic cell death over lytic cell death responses in macrophages. *Cell Death Dis.* **10**, 882 (2019).

25. Dhuna, K. *et al.* Ginsenosides Act As Positive Modulators of P2X4 Receptors. *Mol. Pharmacol.* **95**, 210–221 (2019).

26. Kawano, A. *et al.* Regulation of P2X7-dependent inflammatory functions by P2X4 receptor in mouse macrophages. *Biochem. Biophys. Res. Commun.* **420**, 102–107 (2012).

27. Jonathan Benzaquen, Serena Janho Dit Hreich, Simon Heeke, Thierry Juhel, Salomé Lalvee, Serge Bauwens, Simona Saccani, Philippe Lenormand, Véronique Hofman, Mathilde Butori, Sylvie Leroy, Jean-Philippe Berthet, Charles-Hugo Marquette, Paul Hofman, V. P2RX7B is a new theranostic marker for lung adenocarcinoma patients. *Theranostics* **10**, 10849–10860 (2020).

28. Gilbert, S. *et al.* ATP in the tumour microenvironment drives expression of nfP2X 7 , a key mediator of cancer cell survival. *Oncogene* **38**, 194–208 (2019).

29. Di Virgilio, F. P2RX7: A receptor with a split personality in inflammation and cancer. *Mol. Cell. Oncol.* **3**, (2016).

30. Young, C. N. J. & Górecki, D. C. P2RX7 purinoceptor as a therapeutic target-The second coming? *Front. Chem.* **6**, 248 (2018).

31. Park, J. H. & Kim, Y. C. P2X7 receptor antagonists: a patent review (2010–2015). *Expert Opin. Ther. Pat.* **27**, 257–267 (2017).

32. Gilbert, S. M. *et al.* A phase I clinical trial demonstrates that nfP2X7-targeted antibodies provide a novel, safe and tolerable topical therapy for basal cell carcinoma. *Br. J. Dermatol.* **177**, 117–124 (2017).

33. Agteresch, H. J., Burgers, S. A., Van Der Gaast, A., Wilson, J. H. P. & Dagnelie, P. C. Randomized clinical trial of adenosine 5′-triphosphate on tumor growth and survival in advanced lung cancer patients. *Anticancer. Drugs* **14**, 639–644 (2003).

34. Beijer, S. *et al.* Effect of adenosine 5′-triphosphate infusions on the nutritional status and survival of preterminal cancer patients. *Anticancer. Drugs* **20**, 625–633 (2009).

35. Vijayan, D., Young, A., Teng, M. W. L. & Smyth, M. J. Targeting immunosuppressive adenosine in cancer. *Nat. Rev. Cancer* **17**, 709–724 (2017).

36. Perrot, I. *et al.* Blocking Antibodies Targeting the CD39/CD73 Immunosuppressive Pathway Unleash Immune Responses in Combination Cancer Therapies. *Cell Rep.* **27**, 2411-2425.e9 (2019).

37. Li, X. Y. *et al.* Targeting CD39 in cancer reveals an extracellular ATP-and inflammasome-driven tumor immunity. *Cancer Discov.* **9**, 1754–1773 (2019).

38. Mutini, C. *et al.* Mouse dendritic cells express the P2X7 purinergic receptor: characterization and possible participation in antigen presentation. *J. Immunol.* **163**, 1958–65 (1999).

744 39. Ma, Y. *et al.* ATP-dependent recruitment, survival and differentiation of dendritic cell
745 precursors in the tumor bed after anticancer chemotherapy. *Oncoimmunology* **2**, 5–7 (2013).

746 40. Bours, M. J. L., Swennen, E. L. R., Di Virgilio, F., Cronstein, B. N. & Dagnelie, P. C. Adenosine 5′-
747 triphosphate and adenosine as endogenous signaling molecules in immunity and
748 inflammation. *Pharmacol. Ther.* **112**, 358–404 (2006).

749 41. Kaplanov, I. *et al.* Blocking IL-1β reverses the immunosuppression in mouse breast cancer and
750 synergizes with anti–PD-1 for tumor abrogation. *Proc. Natl. Acad. Sci. U. S. A.* **116**, 1361–1369
751 (2019).

752 42. Okamura, H. *et al.* A novel costimulatory factor for gamma interferon induction found in the
753 livers of mice causes endotoxic shock. *Infect. Immun.* **63**, 3966–3972 (1995).

754 43. Ushio, S. *et al.* Cloning of the cDNA for human IFN-gamma-inducing factor, expression in
755 Escherichia coli, and studies on the biologic activities of the protein. *J. Immunol.* **156**, 4274–9
756 (1996).

757 44. Fabbi, M., Carbotti, G. & Ferrini, S. Context-dependent role of IL-18 in cancer biology and
758 counter-regulation by IL-18BP. *J. Leukoc. Biol.* **97**, 665–675 (2015).

759 45. Segovia, M. *et al.* Targeting TMEM176B Enhances Antitumor Immunity and Augments the
760 Efficacy of Immune Checkpoint Blockers by Unleashing Inflammasome Activation. *Cancer Cell*
761 **35**, 767-781.e6 (2019).

762 46. Zhou, T. *et al.* IL-18BP is a secreted immune checkpoint and barrier to IL-18 immunotherapy.
763 *Nature* (2020). doi:10.1038/s41586-020-2422-6

764 47. Park, S. L., Gebhardt, T. & Mackay, L. K. Tissue-Resident Memory T Cells in Cancer
765 Immunosurveillance. *Trends Immunol.* **40**, 735–747 (2019).

766 48. Sharma, P., Hu-Lieskovan, S., Wargo, J. A. & Ribas, A. Primary, Adaptive, and Acquired
767 Resistance to Cancer Immunotherapy. *Cell* **168**, 707–723 (2017).

768 49. Regala, R. P. *et al.* Atypical protein kinase Cι is required for bronchioalveolar stem cell
769 expansion and lung tumorigenesis. *Cancer Res.* **69**, 7603–7611 (2009).

770 50. Sutherland, K. D. *et al.* Multiple cells-of-origin of mutant K-Ras-induced mouse lung
771 adenocarcinoma. *Proc. Natl. Acad. Sci. U. S. A.* **111**, 4952–4957 (2014).

772

773

Acknowledgments

The authors wish to thank Prof L. Counillon for valuable discussions, Anne Laure Rossi for technical expertise and graphical art. The authors greatly acknowledge the IRCAN's Animal core facility and IRCAN's Flow Cytometry Facility that is supported by FEDER, Ministère de l'Enseignement Supérieur, Région Provence Alpes-Côte d'Azur, Conseil Départemental 06, ITMO Cancer Aviesan (plan cancer), Cancéropole PACA, CNRS and Inserm.

Disclosure of potential conflicts of interest

We have no conflict of interest.

Funding

The funding sources for this work were Institut National du Cancer (INCa), Canceropole PACA, Bristol-Myers Squibb Foundation for Research in Immuno-Oncology, the "Ligue Nationale Contre le Cancer", the French Government (National Research Agency, ANR through the "Investments for the Future": program reference #ANR-11-LABX-0028-01) and the Centre National de la Recherche Scientifique (CNRS),the Institut National de la Santé et Recherche Médicale (INSERM) and the University of Orleans, The Region Centre Val de Loire (2003-00085470), the Conseil Général du Loiret and European Regional Development Fund (FEDER No. 2016-00110366 and EX005756).

Figure legends

Figure 1: HEI3090 enhances ATP-induced receptor channel activity

A. Representation of HEI3090's synthesis steps.

B. Modulation of ATP-induced intracellular Ca^{2+} variation (F1/F0) in HEK mP2RX7 cells (C57Bl/6 origin). After 10 baseline cycles, ATP (333 µm) and HEI3090 (250 nM) were injected.

C. Average Fluo-4-AM fluorescence intensities in HEK mP2RX7 or control HEK pcDNA6 measured 315s after stimulation with ATP (330 µM) and HEI3090 at concentrations ranging from 25 nM to 2.5 µM, as indicated in the color code. Means ± SEM (n=3 independent experiments and 6 replicates).

D. Modulation of ATP-induced TO-PRO-3 uptake in HEK mP2RX7 cells (F1/F0) in cells treated with ATP and HEI3090 (25nM).

E. Average fluorescence intensities in HEK mP2RX7 or control HEK pcDNA6 measured 10 min after stimulation with ATP and HEI3090 at concentrations ranging from 25 nM to 2.5 µM, as indicated in the color code. Means ± SEM (n=3 independent experiments and 6 replicates).

F. Left: Average fluo-4-AM fluorescence intensities in WT or *p2rx7*$^{-/-}$ splenocytes stimulated with 50 µM ATP measured at the plateau i.e. 10 min after stimulation. Means ± SEM (n=2 independent experiments and 4 replicates). Right: Graph represents the percentage of TO-PRO-3 positive cells in splenocytes isolated from naïve WT or *p2rx7*$^{-/-}$ mice. Data are means ± SEM (n=3 independent experiments in duplicate).

G. Pharmacokinetic analysis of HEI3090 intraperitoneally injected in WT mice. Data are means ± SEM (n=3 independent experiments in duplicate). Bars are mean ± SEM. *p<0.05, **p<0.01 ***p<0.001, ****p<0.0001 (Mann-Whitney test). Source data are provided as a Source Data file.

Figure 2: HEI3090 inhibits tumor growth and combined with immunotherapy ameliorates mice survival

A. Prophylactic administration. Average tumor area and weight of LLC allograft after daily treatment with HEI3090. Curves are mean ± SEM.

B. Therapeutic administration. Average tumor area and survival curves of LLC allograft. HEI3090 started when tumors reached 10 to 15 mm^2 of size. Curves are mean ± SEM.

C. Combo treatment. Average tumor area of LLC allograft after HEI3090 and αPD-1 treatment. Spaghetti plots and survival curves of animals are shown.

828 **D.** Schematic illustration of treatment given to LSL *Kras*^{G12D} mice. Representative images showing
829 lung tumor burden. (Bar=2mm upper panel and 500 µm lower panel) with tumor histopathology.
830 Average tumor burden of LSL *Kras*G12D mice in response to treatments were studied as the number
831 of ADC per mouse and the surface of ADC lesions per lung. Each point represents one mouse.
832 *p<0.05, **p<0.01 ***p<0.001, ****p<0.0001 (Mann-Whitney or Mantel Cox (B and C) tests). Source
833 data are provided as a Source Data file.

834

835 **Figure 3: Immune cells mediate the antitumor activity induced by HEI3090**

836 LLC cells were used in all panels except in E.

837 **A.** Average tumor area of LLC allograft in *p2rx7* deficient mice (*p2rx7*$^{-/-}$) after daily treatment with
838 HEI3090 or after adoptive transfer of WT splenocytes and daily treatment with HEI3090

839 **B.** Average tumor area of LLC allograft in *p2rx7* deficient mice (*p2rx7*$^{-/-}$) after adoptive transfer of WT
840 DCs and daily treatment with HEI3090.

841 **C.** Tumor weight of animals from the study shown in A and B.

842 **D.** Characterization of immune infiltrate at day 12. Percentage of CD45^{+} analyzed by flow cytometry
843 among living cells within TME.

844 **E.** Representative picture of CD8^{+} cells recruitment in LSL *Kras*G12D mice. (340X magnification) and
845 quantification.

846 **F.** Representative images of CD3 staining in LLC tumors and quantification.

847 **G.** Percentage of regulatory T cells determined by flow cytometry as FOXP3^{+} CD4^{+} among CD3^{+} within
848 LLC tumors.

849 **H.** Proportion of PMN-MDSC among CD45^{+} within LLC tumors

850 **I.** Gating strategy (left panel) and ratio of NK, CD4^{+} or CD8^{+} T cells on PMN-MDSC within LLC tumors
851 (right panel). data are mean ± SEM. *p<0.05, **p<0.01 ***p<0.001, ****p<0.0001 (Mann-Whitney
852 or two-way Anova (C) tests). Each point represents one individual mouse. Source data are provided
853 as a Source Data file.

854

855 **Figure 4: HEI3090-induced IL-18 production is required to inhibit tumor growth**

856 **A.** Average tumor area of LLC allograft in WT mice injected with IL-1β and IL-18 neutralizing
857 antibodies and daily treatment with HEI3090.

858 **B.** Average tumor area and tumor weight of LLC allograft in *il-18* deficient mice (*il-18*$^{-/-}$) and daily
859 treatment with HEI3090.

C. Representative images of IL-18 staining in LLC tumors.

D. Production of IL-18 and IL-1β in serum of treated mice determined by ELISA.

E. *Ex vivo* production of IL-18 in primary peritoneal macrophages.

F. Representative images of IL-18 staining in lung tumor lesions from LSL *Kras*^{G12D} mice (Bar = 30 µm) and production of IL-18 in serum of LSL *Kras*^{G12D} mice. Data are mean ± SEM. *p<0.05, **p<0.01 ***p<0.001, ****p<0.0001 (Mann-Whitney or Mantel Cox (C) tests or t-test (E). Each point represents one individual mouse. Source data are provided as a Source Data file.

Figure 5: HEI3090 triggers antitumor responses mediated by IL-18-induced NK and CD4$^+$ T cells

A. Average tumor weight of LLC allograft in WT mice injected with depleting antibody and daily treated with HEI3090.

B. Spaghetti plots of LLC allograft in WT mice injected with depleting antibody and daily treated with HEI3090.

C. Average of IFN-γ$^+$ cells among CD45$^+$ cells in LLC tumors.

D. Representative dot plots of IFN-γ and IL-10 staining on TILs (left panel) and ratios of IFN-γ on IL-10 in the same positive cells of each TILs (right panel).

E. *Ex vivo* degranulation assay of splenocytes from LLC tumor bearing mice. CD107a positive cells in NK, CD4$^+$ and CD8$^+$ T cells are shown.

F. Ratios of IFN-γ on IL-10 in the same positive cells of each TILs of IL-18 neutralized mice.

G. Flow cytometry analyses of MHC-I and PD-L1 expression on CD45$^-$ cells in LLC tumors

H. Representative images of PD-L1 staining in cancer lesion of LSL *KRas*^{G12D} mice. (Bar = 30 µm) and quantification. Bars are mean ± SEM. Each point represents one individual mouse. *p<0.05, **p<0.01 ***p<0.001, ****p<0.0001 (Mann-Whitney test). Source data are provided as a Source Data file.

Figure 6: HEI3090 combined with αPD-1 induces antitumor memory immune response

A. Schematic illustration of treatments with transfer of CD8 cells.

B. Average tumor area of LLC allograft in 90 days-old WT and 90 days-old cured mice in absence of treatment.

C. Survival curves of animals from the study shown in B

D. Average tumor area of LLC allograft in WT mice injected with CD8$^+$ T cells isolated from re challenged cured mice as shown in A

892 **E.** Long lasting antitumor immune response: schematic illustration of treatments

893 **F**. Mouse body weight follow up of 300 days-old cured mice injected with anti-isotype (black circle) or
894 depleting αCD8 antibodies (blue circle).

895 **G**. Individual survival curves of 340 days-old WT and cured animals injected with anti-CD8 antibody
896 and re challenge with LLC in absence of treatment.

897 **H.** Average tumor area from animals shown in G.

898 **I.** Survival curves from animals shown in G. Data are mean ± SEM. *p<0.05, **p<0.01 ***p<0.001,
899 ****p<0.0001 Mann-Whitney, two-way Anova or Mantel Cox tests. Source data are provided as a
900 Source Data file.

901

902 **Figure 7: P2RX7 expression in LUAD is associated with "Hot" immunophenotype signature**

903 **A.** Association of *P2RX7* mRNA expression with a cluster of inflammatory genes (heatmap).

904 **B.** GSEA plot associating *P2RX7* high mRNA levels from LUAD patients (TCGA) with three
905 inflammatory signatures.

906 **C.** Correlation curves of *P2RX7* and *CD274* expression from LUAD patients (TCGA) of all stage (left
907 panel), low stage (middle panel) and high stage (right panel). Mann-Whitney or Mantel Cox (C and E)
908 tests were used to performed statistical analyses.

909 **D.** Kaplan Meyer plot (http://kmplot.com) showing survival curves of *P2RX7* high vs *P2RX7* low
910 patients (left panel), *CD274* high vs *CD274* low (middle panel) and *P2RX7* high or low vs *CD274* high
911 or low (right panel). For all panels, the optimal cut-off is determined on KMplot. The *P*-value (log-rank
912 (Mantel Cox) test), the hazard ratio and number of patients are indicated. Source data are provided
913 as a Source Data file.

914

915

916

917 **Table 1: Antibodies used to phenotype immune cells**

Antibody	Company	Clone	Species	Isotype	Fluorochrome	Stock concentration	Dilution
CD16/CD32 Fc Block	BD Biosciences	2.4G2	Rat SD (outbred)	IgG_{2b}, κ	Uncoupled	0.5mg/ml	1/100
CD3ε	BD Biosciences	145-2611	Armenian Hamster	IgG_1, κ	PerCP-Cy5.5	0,2mg/ml	1/100
CD4	Biolegend	GK1.5	Rat	IgG_{2b}, κ	AF647	0.5 mg/ml	1/100
CD4	BD Biosciences	GK1.5	Rat LEW	IgG_{2b}, κ	PE	0,2mg/ml	1/100
CD4	BD Biosciences	RM4-5	Rat DA	IgG_{2a}, κ	BV711	0,2mg/ml	1/100
CD8α	Biolegend	53-6.7	Rat	IgG_{2a}, κ	BV650	50 ug/ml	1/100
CD8α	BD Biosciences	53-6.7	Rat LOU	IgG_{2a}, κ	BV650	0,2mg/ml	1/100
γδ TCR	BD Biosciences	GL3	Armenian Hamster	IgG_2, κ	PE	0,2mg/ml	1/100
CD25	BD Biosciences	PC61	Rat OFA	IgG_1, λ	V450	0,2mg/ml	1/100
CD44	BD Biosciences	IM7	Rat	IgG_{2b}, κ	APC	0,2mg/ml	1/100
CD44	BD Biosciences	IM7	Rat	IgG_{2b}, κ	PE-Cy7	0,2mg/ml	1/100
CCR7	BD Biosciences	4B12	Rat LOU	IgG_{2a}	PE-CF594	0,2mg/ml	1/100
CD107a	BD Biosciences	1D4B	Rat SD (outbred)	IgG_{2a}, κ	PE-Cy7	0,2mg/ml	1/100
NK1.1	BD Biosciences	PK136	Mouse C3H x BALB/c	IgG_{2a}, κ	PE-CF594	0,2mg/ml	1/100
B220	eBiosciences	RA3-6B2	Rat	IgG_{2a}, κ	FITC	0.5 mg/ml	1/200
CD19	BD Biosciences	ID3	Rat LEW	IgG_{2a}, κ	FITC	0.5 mg/ml	1/100
CD45.2	BD Biosciences	104	Mouse SJL	IgG_{2a}, κ	BV786	0,2mg/ml	1/100
CD11b	eBiosciences	M1/70	Rat	IgG_{2b}, κ	APC	0,2mg/ml	1/400
CD11c	BD Biosciences	HL3	Armenian Hamster	IgG_1, λ2	PE-Cy7	0,2mg/ml	1/100
Ly6C	BD Biosciences	AL-21	Rat	IgM, κ	V450	0,2mg/ml	1/100
Ly6G	BD Biosciences	1A8	Rat LEW	IgG_{2a}, κ	AF700	0,2mg/ml	1/100
Ly6G	BD Biosciences	1A8	Rat LEW	IgG_{2a}, κ	FITC	0,5mg/ml	1/100
CD80	Biolegend	16-10A1	Armenian Hamster	IgG	PE	0,2mg/ml	1/100
CD86	BD Biosciences	GL1	Rat LOU	IgG_{2a}, κ	AF700	0,2mg/ml	1/100
CD86	BD Biosciences	GL1	Rat LOU	IgG_{2a}, κ	APC	0,2mg/ml	1/100
I-A/I-E	Biolegend	M5/114.5.2	Rat	IgG_{2b}, κ	APC/fire 750	0,2mg/ml	1/100
$H\text{-}2K^b/H\text{-}2D^b$	Biolegend	28-8-6	Mouse (C3H)	IgG_{2a}, κ	FITC	0.5mg/ml	1/100
IL-10	BD Biosciences	JES5-16E3	Rat	IgG_{2b}, κ	BV421	0,2mg/ml	1/100
Foxp3	eBiosciences	FJK16S	Rat	IgG_{2a}, κ	PE	0,2mg/ml	1/100
CD103	Biolegend	2E7	Armenian Hamster	IgG	PerCP-Cy5.5	0,2mg/ml	1/100
IFN-γ	BD Biosciences	XMG1.2	Rat	IgG_1, κ	APC	0,2mg/ml	1/100
IL-17A	BD Biosciences	TC11-18H10	Armenian Hamster	IgG_1, κ	AF700	0,2mg/ml	1/100
IL-4	BD Biosciences	11B11	Rat	IgG_1	BV711	0,2mg/ml	1/100
IL-13	eBiosciences	eBio13A	Rat	IgG_1, κ	AF488	0.5 mg/ml	1/100
GATA3	BD Biosciences	L50-823	Mouse BALB/c	IgG_1, κ	BV421	0,2mg/ml	1/100
CD279 (PD-1)	BD Biosciences	J43	Rat	IgG_{2a}, κ	APC	0,2mg/ml	1/100
CD274 (PD-L1)	Biolegend	10F.9G2	Rat	IgG_{2b}, κ	APC	0,2mg/ml	1/100
CD274 (PD-L1)	Biolegend	10F.9G2	Rat	IgG_{2b}, κ	BV421	100µg/ml	1/100
CD273 (PD-L2)	Biolegend	TY25	Rat	IgG_{2a}, κ	PE/dazzle 594	0,2mg/ml	1/100
CTLA-4	BD Biosciences	UC10-4F10-11	Armenian Hamster	IgG_1, κ	PE	0,2mg/ml	1/100
TIM-3	BD Biosciences	5D12/TIM-3	Mouse	IgG_1, κ	PE	0,2mg/ml	1/100
P2RX7	Biolegend	1F11	Rat	IgG_{2b}, κ	PE	0,2mg/ml	1/8

918

919

Figure 1

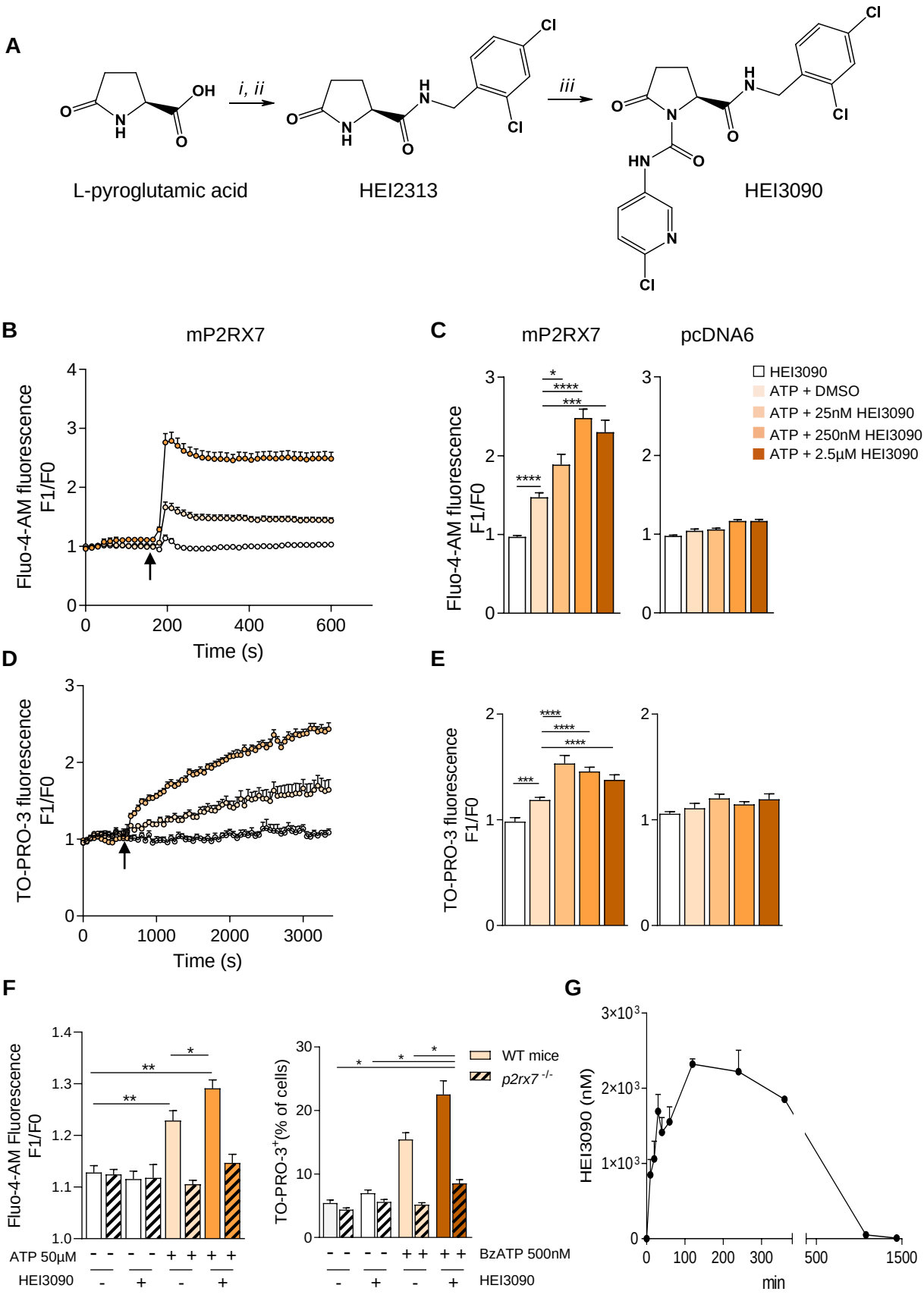

Figure 2

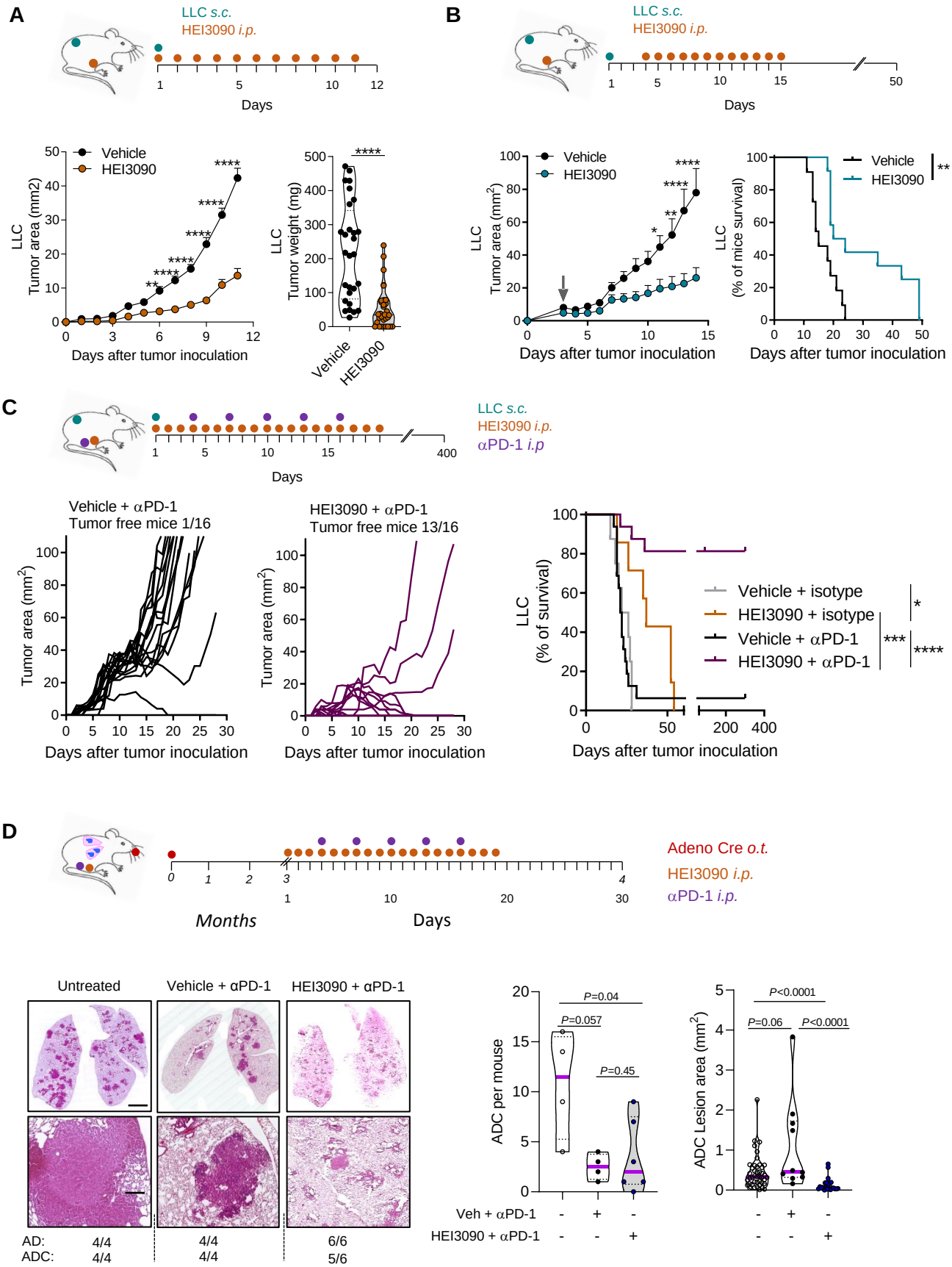

Figure 3

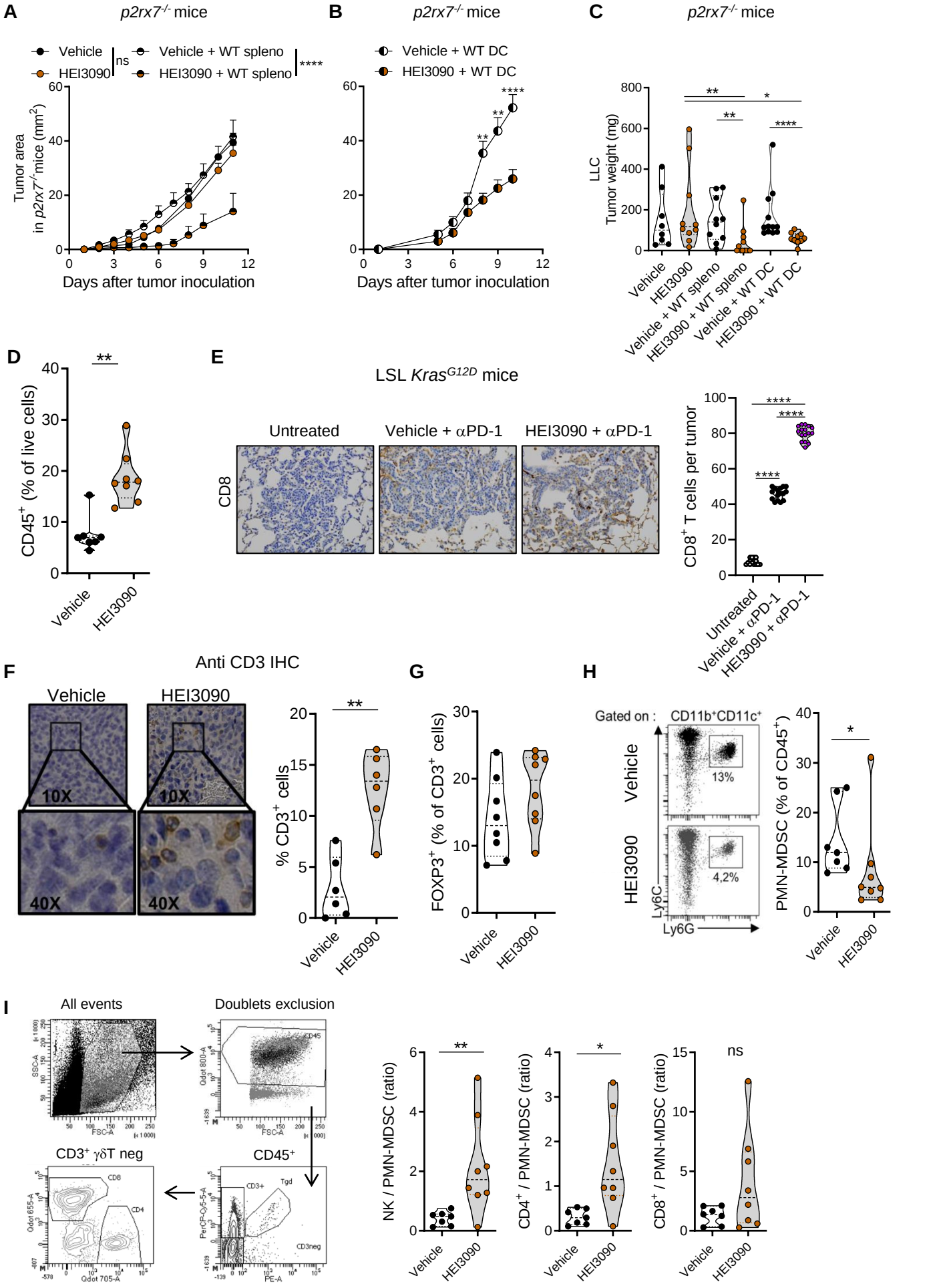

Figure 4

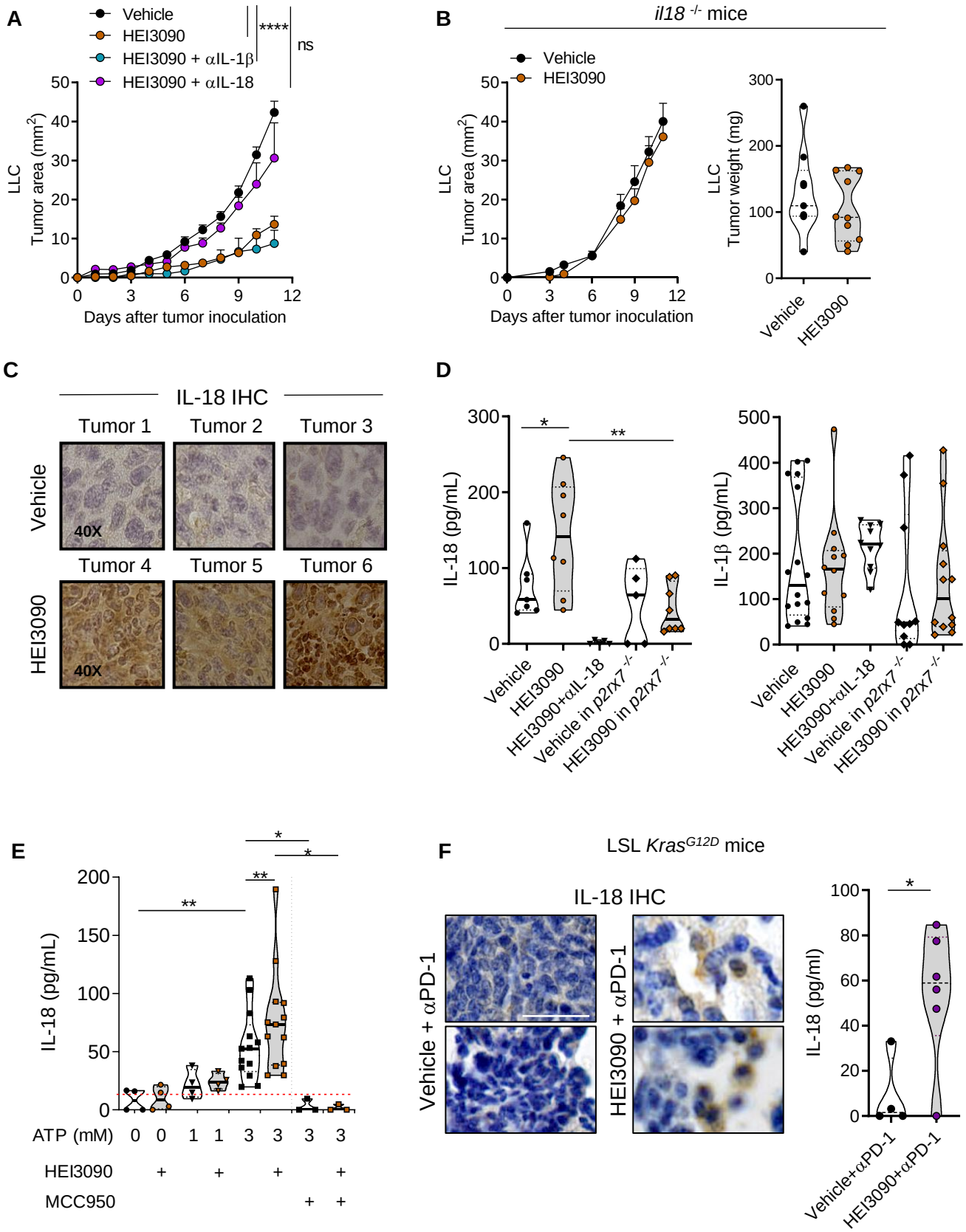

Figure 5

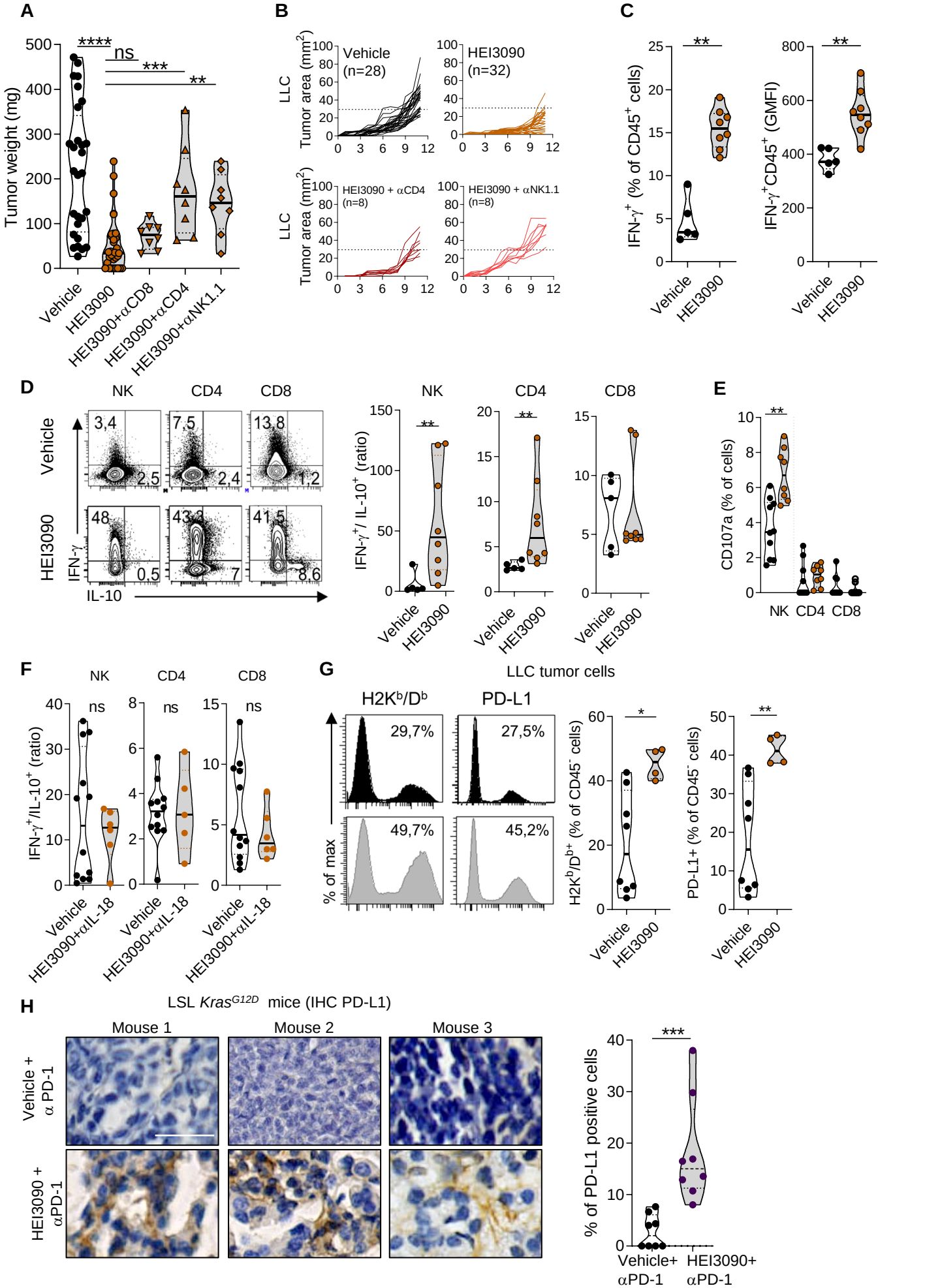

Figure 6

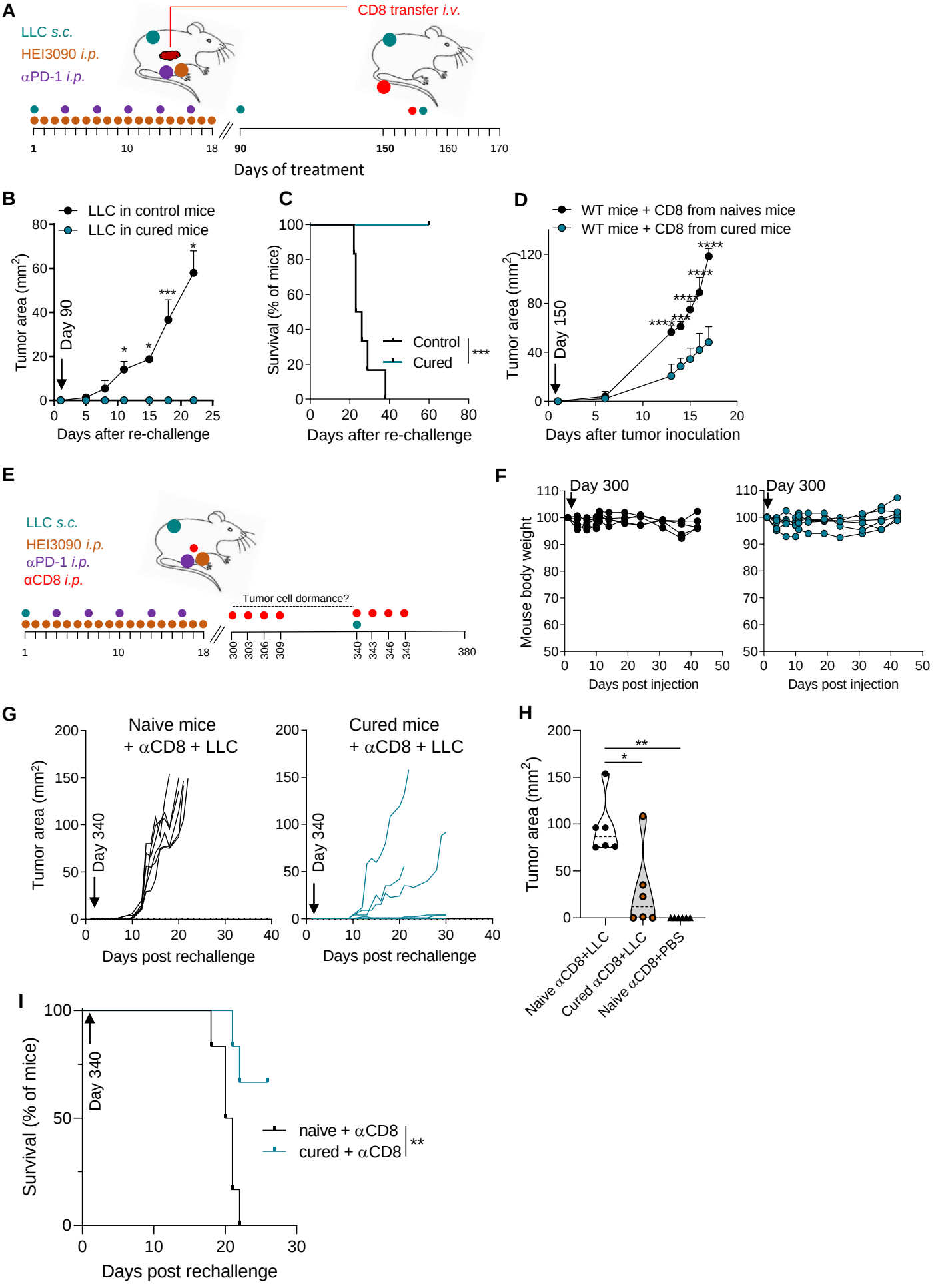

Figure 7